BioSystems 206 (2021) 104450

Contents lists available at ScienceDirect

BioSystems

journal homepage: www.elsevier.com/locate/biosystems

A multi-scale agent-based model for avascular tumour growth

Sounak Sadhukhan [a,*], P.K. Mishra [a], S.K. Basu [a], J.K. Mandal [b]

[a] Department of Computer Science, Banaras Hindu University, Institute of Science, Varanasi 221005, India
[b] Department of Computer Science and Engineering, University of Kalyani, West Bengal 741235, India

ARTICLE INFO

Keywords:
Multi-scale model
Avascular tumour growth
Signalling pathway
Agent based model

ABSTRACT

In this paper, we have developed a multi-scale, lattice-free, agent based model of avascular tumour growth in epithelial tissue. The model integrates different events to identify the underlying diversity within intracellular, cellular, and extracellular layer dynamics. The model considers every cell as an agent. A cellular agent may proliferate, spawns two identical daughter agents, or it may be transformed into other phenotypes during its life time depending on its internal proteins' activity as well as its external microenvironment. In this context, a simplified age-structured cell cycle model is adopted from the existing literature. The model considers that the intracellular events are regulated by p27 gene expression. In this model, p27 protein controls the overall tumour growth dynamics. Moreover, p27 is controlled by the external oxygen and nutrients that are modelled with the reaction-diffusion equations. The model also considers several biophysical forces which directly effect on the tumour growth dynamics.

This modelling framework offers biologically realistic outcomes and also covers important criteria of the hallmarks of cancer which include oxygen and nutrient consumptions, micro-environmental heterogeneity, tumour cell proliferation by avoiding growth suppressor signals, replication of tumour cells at an abnormally faster rate, and resistance of apoptosis. The avascular tumour growth model is validated with immunohistochemistry and histopathology data. The outcome of the proposed model is very close to the range of the patient data, which concludes that the model is capable enough to mimic these complex biophysical phenomena.

1. Introduction

The growth of a solid tumour can be categorized as: avascular, angiogenesis, and vascular phase (Folkman (1985)). In avascular phase, tumour depends on its surrounding microenvironments for absorbing oxygen, and necessary nutrients as it do not have direct blood vessel support (Folkman (1987)). The nutrients and oxygen are transported to and from the extracellular matrix (ECM) through passive diffusion (Sutherland (1988)). Therefore, growth of a tumour is restricted in this phase. To grow further, tumour must undergo angiogenesis for having sufficient nutrients and oxygen (Folkman (1974); Folkman (1976); Muthukkaruppan et al., 1982). Most of the processes underlying avascular tumour growth are not properly understood yet. Mathematical models can enhance the understanding of the processes underlying during the avascular phase.

Tumour growth is very complex, multi-layered, and multi-phase phenomenon. It is a collection of coordinated, concurrent, and interactive events across different spatial and temporal scales. For example, at the tissue layer, nutrients and oxygen diffuse through the ECM and regulate the tumour cell growth and its division (Sutherland (1988)). On the other hand, at the intracellular layer, the cell cycle is controlled by some molecular signals (Tyson and Novak (2001)) which are also regulated by the surrounding nutrients and oxygen levels. Moreover, depending upon different molecular interactions and metabolism criteria, tumour cells mutate into different phenotypes which can be observed at the cellular layer (Macklin et al., 2012). Therefore, scientists are still trying to explore cancer by integrating the events of different layers like, molecular, cellular, and tissue.

In multi-layered dynamical system, any changes in the lower layers leads to propagate its effects to the layers above it; on the other hand, modification in higher layers in turn puts impact on the subsequent lower layers. As an example, molecular activities (intracellular layer) directly effect on tumour cell behaviour (cellular layer), whereas the impact of nutrient concentration changes (tissue scale) affect the cellular metabolism (intracellular layer) as well. Besides the propagation of signalling molecules from the intracellular to extracellular and from the

* Corresponding author.
E-mail addresses: sounaks.cse@gmail.com (S. Sadhukhan), mishra@bhu.ac.in (P.K. Mishra), swapankb@gmail.com (S.K. Basu), jkm.cse@gmail.com (J.K. Mandal).

https://doi.org/10.1016/j.biosystems.2021.104450
Received 2 August 2020; Received in revised form 27 May 2021; Accepted 31 May 2021

extracellular to intracellular, some physical forces are also applied on tumour cells simultaneously which have a great impact on tumour growth dynamics. Therefore, better understanding of tumour initiation and its progression requires the descriptions and integrations of all the events at multiple spatial and temporal scales. These interconnected dynamic phenomena can only be captured through multi-scale modelling that can combine multiple spatial and temporal scales simultaneously.

In this paper, an agent based model (ABM) for describing the growth of avascular tumour growth is developed. ABM consists of multiple autonomous entities that mimics the behaviour of a dynamical system like tumour growth. The autonomous decision making entities can be easily combined with ordinary differential equations (ODEs) and partial differential equations (PDEs) for representing a system environment (hybrid modelling). In the context of avascular tumour growth modelling, every tumour cell act as a cellular agent that must follow certain rules which define its behaviour during the interactions with the neighbouring cellular agents and the surrounding microenvironment. A cellular agent may grow, enter into proliferative or hypoxic or quiescent states, spawn new daughter cells, and undergo apoptosis or necrosis in responds to the niche. Multi-scale ABM is very much useful for integrating many spatiotemporal scales (from intracellular layer to the tissue layer) and for recognizing the underlying diversity within the extracellular, cellular, and intracellular dynamics. It also helps to quantify the relationship between intracellular properties of individual tumour cells, its microenvironment, and the tumour morphology.

Modelling of intracellular level describes a variety of interactions among various molecules, for example, the effects of the extracellular nutrients and oxygen molecules in tumour cell metabolism, the effects of autocrine and paracrine signalling molecules in cell cycle, etc. The interactions among these molecules happen in the smallest spatial scale (*e.g.*, nanometre (nm)) as well as temporal scales (*e.g.*, nanosecond (ns) to microsecond (μs)). Researchers generally use ODEs to represent the rate of change of these signalling concentrations with respect to time. On the other hand, cellular scale modelling involves the phenotypic changes of tumour cells during its life time due to its microenvironment and metabolism dynamics. It may also describe the movement of cells caused not only by phenotypic changes, but also due to its interactions with the neighbouring cells. Interactions between tumour cells and phenotypic changes can take few minutes to hours and happen within micrometres (μm) distance. Tissue layer modelling deals with the phenomena like diffusion of nutrients and oxygen from the sources, or diffusion of several chemical substrates by the tumour cells, etc. that span over the entire tumour tissues. These events take few hours to days and happen over millimetre (mm) to centimetre (cm) scales and can be described using a series of PDEs. These PDEs also consider the consumption of nutrients and oxygen as well as the productions of chemical substrates by the cellular agents.

Over the last two decades, multi-scale modelling is frequently used for understanding the tumour growth and its progression. Intricacies of most of the bio-chemical and bio-physical phenomena regarding tumour microenvironment are less understood. Researchers have developed various multi-scale models to describe various phases of tumour growth from different perspectives. Jiang et al. (2005) have developed a three-scale hybrid model to describe the complexity of avascular tumour microenvironment. The sub-cellular layer of the model, which consists of various types of growth promoters and inhibitory factors, is controlled by a Boolean network. The cellular dynamics is described by a lattice Monte Carlo model. The model predicts the microenvironment which helps the tumour spheroid to survive. Ribba et al. (2006) have investigated the failure of an anti-metastatic therapeutic agent named matrix metalloproteinases inhibitor (MMPI) which was developed in early 90's by a pharmaceutical company for inhibiting tumour growth and metastatic progression. In this context, they have developed a multi-scale continuum model which integrates age-structured cell cycle model and studied the roles of MMPs in cancer growth. The model considers proliferative and quiescent cells, where the spatial dynamics of the tumour is maintained with the Darcy law. The model assesses the quality of the anti-metastatic therapy and predicts the reasons of ineffectiveness of the therapy in advanced cancer patients.

Zhang et al. (2007) have presented a multi-scale ABM for describing complex brain tumour microenvironment. They have considered each tumour cell as an agent. Every cellular agent is equipped with an epidermal growth factor receptor (EGFR) gene-protein interaction module connected with a simplified cell cycle description. The model illustrates that, the proliferative and motile cell population oscillate over the time, putting direct effects on the spatiotemporal dynamics of the tumour. Macklin et al. (2009) have established a multi-scale model for solid tumour growth by combining its avascular growth, tumour angiogenesis and vascular growth. The model illustrates the relation between the tumour growth, vascular network remodelling, and the blood flow through the network. The model also shows that, the ECM degradation by the tumour cells have tremendous effects on vascular network expansion as well as tumour growth response. The model demonstrates that the newly developed blood vessels have encapsulation tendency rather than penetration.

Li et al. (2013) have developed a 3-D multi-scale model of tumour growth based on stem cell concept to investigate tumour development and drug response. The model considers cancer stem cells, progenitor cells, and differentiated cells together with complex microenvironment. The model shows that, some portion of cancer stem cells play a crucial role in tumour progression and drug resistance. It also illustrates that, a pure chemo-drug treatment increases the population of cancer stem cells, that leads to the failure of the treatment. Chaplain and Powathil (2016) have studied the effects of cell cycle, phase specific chemotherapy on the tumour growth by developing two hybrid multi-scale tumour growth models with incorporation of multiple interactions present in the sub-cellular, cellular, and extracellular spaces. Peng et al. (2017) have investigated the tumour dynamics and tumour morphology at tissue scale by incorporating the effects of urokinase plasminogen activator (uPA) which helps the tumour in tissue invasion.

All the researches mentioned above did not consider the effects of physical forces on tumour growth dynamics. Even most of them ignore the cellular movement in their research. Also most of the researches have considered that the duration of cell cycle is static (except Zhang et al. (2007); Chaplain and Powathil (2016)). But in reality, cell cycle time may vary depending on its surrounding microenvironment. In this paper, we develop a multi-scale agent based model for avascular tumour growth (solid tumour) in epithelial tissue by integrating the intracellular, cellular, and tissue (extracellular) layer events. Here, each tumour cell acts as an agent. At the intracellular layer, cell cycle of cancer cells has been taken care of. As, the cell cycle can be described with many potential pathways, this study considers one of them for the purpose of modelling.

Cell cycle is controlled by different types of intracellular proteins like, cadherin-1 (cdh-1), cyclin, cyclin-dependent kinases (CDKs), and extracellular oxygen and nutrient. In general, the level of p27 in tumour cells is very low. But hypoxia (deficiency of oxygen and nutrients) triggers the up regulations of p27 protein within tumour cells. If the p27 expression exceeds a certain threshold, then the state of the tumour cell transforms into a hypoxic one. After a certain time, the hypoxic cell turns into necrotic. In this paper, a simple mathematical model for cell cycle is adopted (Alarcón et al., 2004). The model considers that, during cell cycle, concentration of p27 protein decides the fate of a tumour cell. The model also assumes that, p27 acts as an inhibitor of p53 protein (tumour suppressor protein) which is responsible for cell apoptosis. These protein interactions have been occurred in ns-μs time within nm space. The interactions of intracellular protein are modelled with a system of ODEs.

The model assumes that, an avascular tumour cell transforms into different phenotypes (proliferative, quiescent, hypoxic, necrotic, and apoptotic) during its life time. The phenotypic changes not only depend

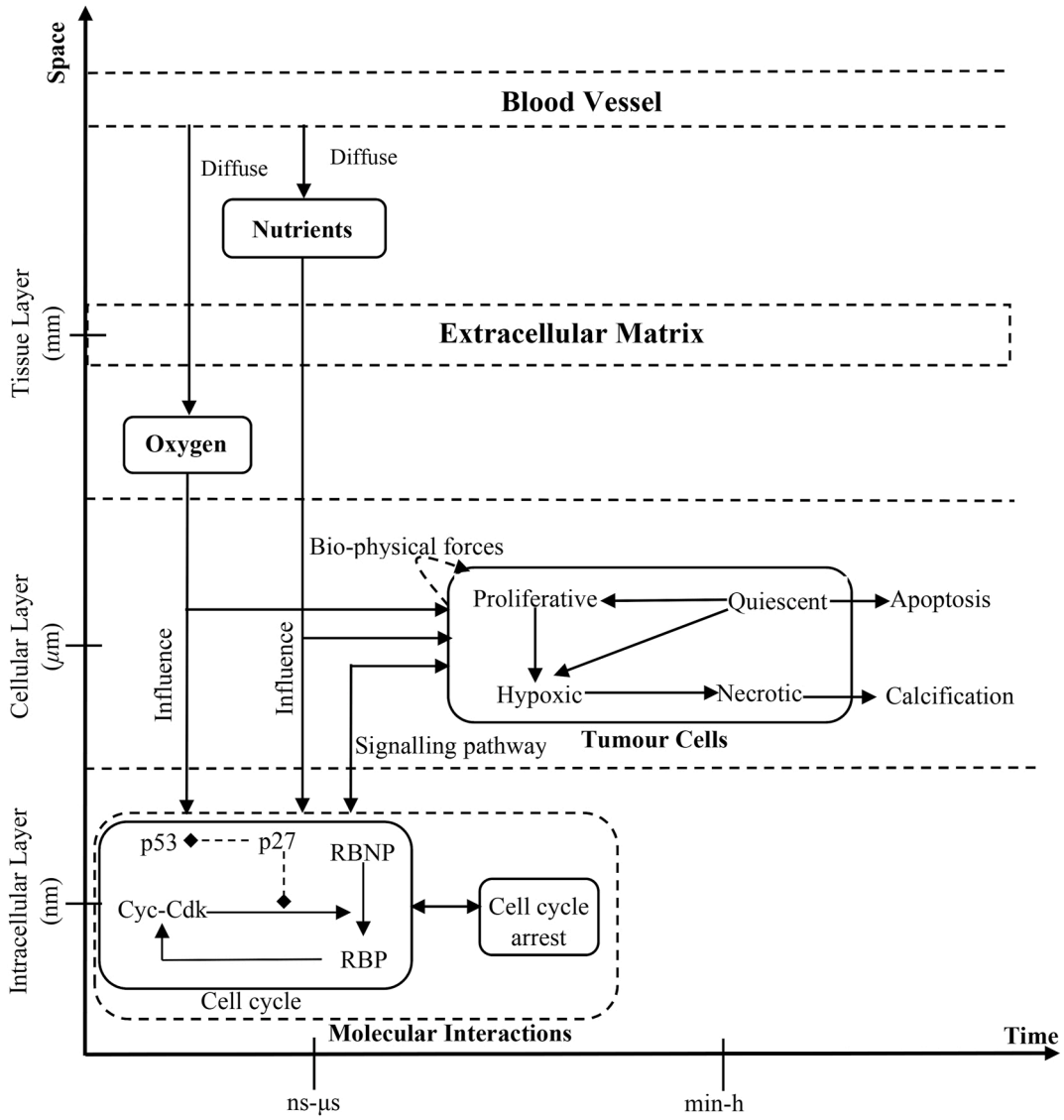

Fig. 1. Multi-scale model framework for avascular tumour growth from the perspective of tumour cells which contains the interacting events that span across intracellular, cellular, and tissue scales. Arrow sign indicates influence or control or regulatory or inhibitory behaviour.

on its cell cycle but also on its neighbourhood, and the surrounding oxygen and nutrient levels. In this research, it is considered that, every tumour cell is in quiescent state at the initial phase of the cell cycle. Depending on its microenvironment, it may change itself into proliferative or hypoxic or apoptotic one. A tumour cell interacts with its microenvironment through the surface receptors. The surface receptors of tumour cells regulate gene expression through complex signals. Also, the gene expression pattern dictates the production and balance of proteins within the cells. Hence, a complex interaction exists between cancer cells and its surroundings for controlling the cell cycle and cell growth (Clyde et al., 2006). The interaction among the tumour cells and the microenvironment creates several physical forces (cell-cell interaction force, chemotactic force, drag force etc.) which directly effect on the tumour cell dynamics, and help to move tumour cells in the domain space freely (lattice free model). These phenomena play an important role in tumour evolution and its growth dynamics. In this research, it is considered that, movements in the avascular tumour cells can be observed only due to the applied physical forces; no phenotypic changes are responsible for these movements. The events in the cellular layer happen in min-h time over μm distance.

At the tissue layer, the model considers heterogeneous microenvironment which contains tumour cells, and the pre-existing blood vessels. The blood vessels release nutrients and oxygen which diffuse towards the tumour. Nutrients and oxygen are crucial factors for maintaining the cell cycle. The events in the tissue layer happen in minutes to hour over mm to cm distance. These events are modelled with a couple of PDEs.

The events in intracellular and tissue scale are combined with the events of cellular scale through ABM modelling (hybrid approach). The integrated system is simulated with the values, mostly found from the previous studies. However, the values of few parameters come from the phenomenological arguments as its values are very difficult to find out. A schematic framework of the model is described pictorially in Fig. 1. The model describes the key criteria of the hallmarks of cancer (Hanahan and Weinberg (2000); Hanahan and Weinberg (2011)) which includes oxygen and nutrients consumption, multicellular heterogeneity, tumour cell proliferation by avoiding growth suppressor signals, replication of cells at an abnormally faster rate, and resistance of apoptosis.

This paper is organized as follows: Section 2, 3, and 4 describe the models of intracellular, cellular, and tissue layer respectively. Section 5 shows the integration of these events across different spatial as well as temporal sales and the simulations of the model with different

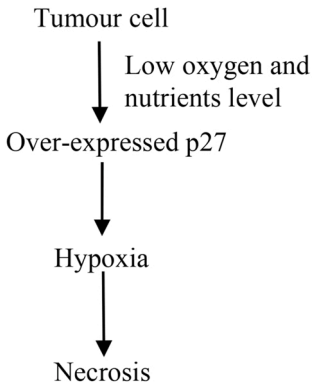

Fig. 2. Transformation of tumour cell due to low oxygen and nutrients level.

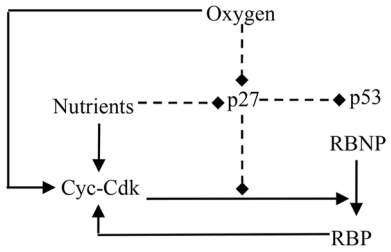

Fig. 3. Schematic diagram of tumour cell cycle model. The directed arrows represent the activator signals whereas the diamond shaped dotted arrows represent the inhibitory control signal.

microenvironments; Section 6 discusses the validation of the model and concludes this paper.

2. Intracellular layer modelling

Most of the activities in the living organisms are performed inside the cells. Each cell contains a nucleus which is bounded by cytosol and wrapper within bi-lipid membrane (cell membrane). Cell membrane guards the cell from the surrounding environment and keep the pH and other chemical levels in balance by exchanging signalling molecules with the neighbouring cells and the surrounding microenvironment. These signalling molecules play a key role to maintain an equilibrium with the surrounding microenvironment by regulating cell cycle speed through utilizing growth inhibitory signals (GISs). These GISs are further controlled by the interactions between cyclin and cyclin-dependent kinases (CDKs). In tumour cell, balance between the signalling molecules is no longer exist. Therefore, an unbounded and uncoordinated cell growth can be seen.

In the next subsections, the molecular signals which influence the cell cycle are discussed in brief. Influences of cell cycle in the tumour formation, and progression are also illustrated in below (in subsection 2.1). subsection 2.2 describes the modelling of cell cycle with a system of ODEs.

2.1. Cell cycle and tumour progression

Cell growth is controlled by cell cycle which consists of a series of highly decorated and interlinked steps. These steps can be grouped into four primary sections: 'G1' (gap 1), 'S' (synthesis), 'G2' (gap 2), and 'M' (mitosis). Further, the 'M' phase is composed of two tightly coupled processes: mitosis and cytokinesis. In the initial phase ('G1'), cell proliferation, protein synthesis are performed and the cell becomes ready for the DNA replication. In the second phase ('S'), the DNA replication is accomplished while in the 'G2' phase cell nucleus prepare for the division. In mitosis, cell's nucleus is divided first and then the cytoplasm of the cell is divided (in cytokinesis) into two daughter cells.

There are multiple check points exist across the phases in the cell cycle such as, 'G1/S' check point, 'S/G2' check point, and 'G2/M' check point. Among these check points, 'G1/S' and 'S/G2' examine the intrinsic signals (like genetic irregularities) of a cell. These two check points are regulated by CDK1 and CDK2. Besides these checkpoints, another check point ('R') exists in between the early and late 'G1' which examines both intrinsic and extrinsic signals (Orford and Scadden (2008)). 'R' (restriction) check point divides the 'G1' phase into mitogen dependent (early 'G1') and mitogen independent (late 'G1') phase. It indicates the irreversible transition of a cell after which it must enters into the cell cycle and the mitogenic signals are no longer required.

In the early phase of 'G1', absence of mitogenic stimuli helps a cell to exit from the cell cycle and it becomes quiescent ('G0'). In quiescent state, cells remain alive, being small in size with low metabolic activity. At the initial phase of cell cycle ('G1'), anaphase protein complex (APC) is activated and it down regulates cyclins using proteolytic molecules. APC is made of couple of polypeptides and two type of proteins: Cdc20 and Cdh1. The CDKs remain inactive throughout the 'G1' phase and its production are being degraded because of down regulation of cyclins. But as soon as the synthesis of cyclins are up regulated at the starting of the 'S' phase, cycins activate its associated CDKs which remain high in the rest of the phases in the cell cycle. On the other hand, cyclin-CDK activates Cdc20 but inhibits Cdh1.

There are remarkable differences between the cell cycle of noncancerous and cancerous cells. Cell cycle is not only influenced by the internal signalling molecules but also the surrounding microenvironments, especially, the level of nutrients and oxygen. Hypoxic condition up regulates the p27 expression which influences the cell cycle, though its level remains comparatively low in a normoxic tumour cell than a noncancerous healthy cell (Alarcón et al., 2004). In noncancerous cells, up regulation of p27 induce apoptosis (Alarcón et al., 2004), while cancerous cells react differently in hypoxic situation. It is already found that, reduction of nutrients and oxygen alter the phenotype of a tumour cell into hypoxic state (Royds et al., 1998). Hypoxic tumour cells can resist intense level of p27 and it remain alive, though some genetic changes occur due to reduction of oxygen and nutrient levels (Alarcón et al., 2004). In this research, it is considered that, after a certain time duration the hypoxic tumour cells turn into necrotic (Fig. 2).

Clinically, hypoxia is one of the major reasons for the evolution of tumour growth and its progression. In avascular phase, tumour cells in hypoxic state secrete a number of TAFs which initiate angiogenesis. Angiogenesis acts as a bridge between the avascular and vascular phase of the tumour. It is very crucial process for the tumour cell invasion and metastasis.

2.2. Cell cycle model

The cell cycle is controlled by the cytoplasmic proteins like, cyclin, CDKs, APC, and the extracellular nutrients, and oxygen molecules. It is already found that, hypoxia is one of the reasons for the prolonged cell cycle of tumour cell (Gardner et al., 2001). Regulators of CDK2, particularly cyclin E and p27 are well influenced by the hypoxia. The overexpressed p27 supress the activities of cyclin-CDK which delay the cell cycle progression. Further, the activation of retinoblastoma protein (RB) through cyclin-CDK is also supressed by p27 (Fig. 3). The model considers that, if the level of p27 increases beyond a certain threshold, then the cell would be transformed into hypoxic state and it will have prolonged cell cycle. After a time period, the hypoxic cell turns into necrotic.

In this paper, a simplified age-structured cell cycle model, based on one of the potential pathway, is incorporated. In this context, we adopt the cell cycle model of Alarcón et al. (2004) and modify it to include the impacts of oxygen and nutrients on avascular tumour growth. The model considers that oxygen and nutrients work as inhibitors of p27 protein as

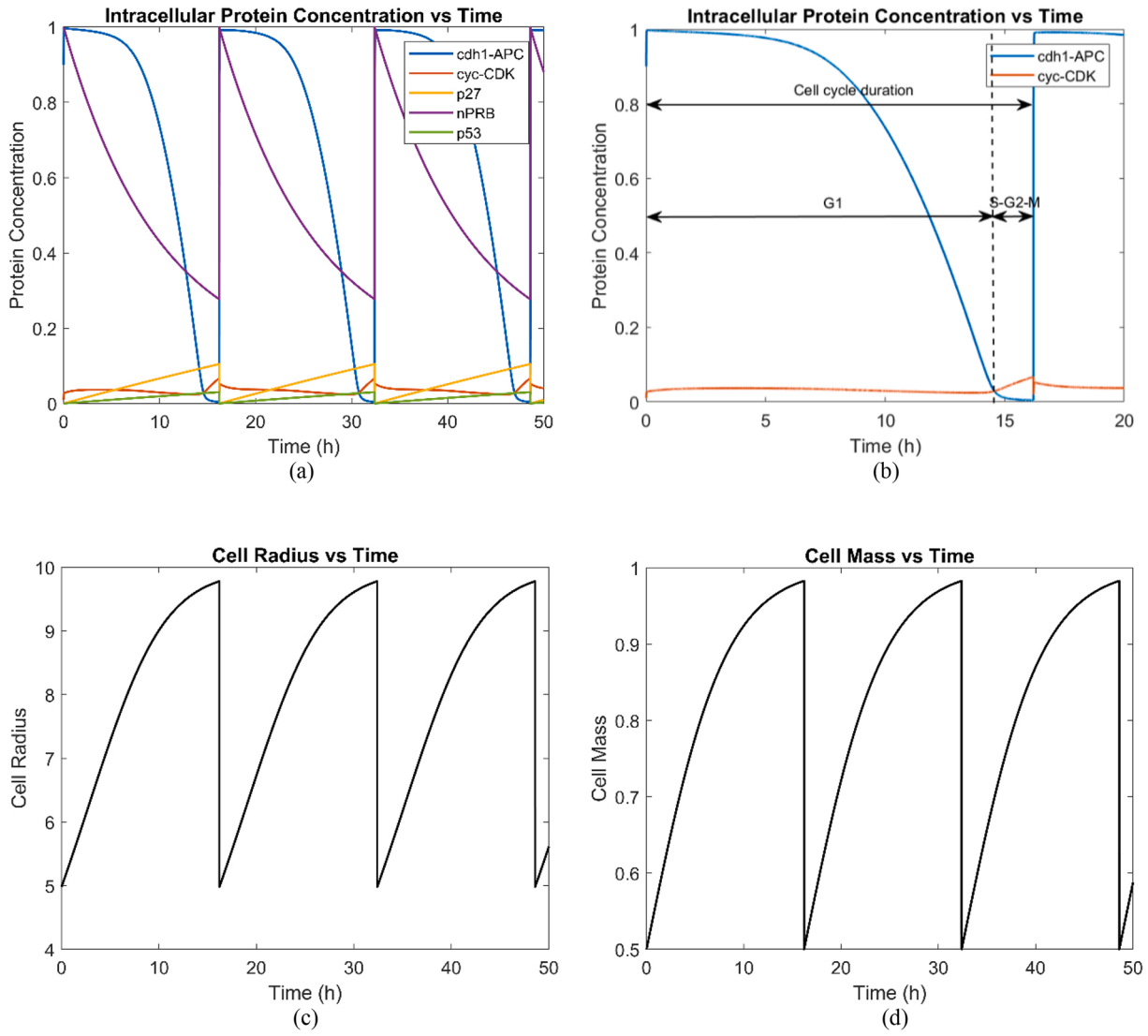

Fig. 4. (a) Represents the dynamics of intracellular proteins during the tumour cell cycle; (b) dynamism of Cdh1-APC and cyclin-CDK during 'G1' and 'S-G2-M' phases; (c) represents cell radius changes during the cell cycle; (d) represents cell mass changes during the cell cycle. The computation has done with the values mentioned in Table 1, $C_N = 1$, and $C_O = 1$.

well as activators of cyclin-CDK (Fig. 3). Further, it is considered that, p27 acts as an inhibitory regulator of p53 protein in tumour cells (Choi et al., 2003) (Fig. 3). The model assumes that, the radius (R) and mass (m) of a tumour cell are regulated by the cell cycle. Please note that, the tumour cell radius R is different from the check point 'R' in the cell cycle.

The model considers Cdh1-APC as [cdh1-APC], cyclin-CDK as [cyclin-CDK], p27 as [p27], nPRB as [nPRB], p53 as [p53], cell radius as R, and cellular mass as m. The set of ODEs governing the simplified tumour cell cycle model with the above considerations are following,

$$\frac{d[\text{cdh1}-\text{APC}]}{dt} = \frac{1+k_1[\text{nPRB}]}{J_3+1-[\text{cdh1}-\text{APC}]} - \frac{k_2 R[\text{cdh1}-\text{APC}][\text{cyc}-\text{CDK}]}{J_4+[\text{cdh1}-\text{APC}]} \tag{1}$$

$$\frac{d[\text{cyc}-\text{CDK}]}{dt} = k_3\frac{(1+\alpha.C_O.C_N).C_O.C_N}{K_{[\text{cyc}-\text{CDK}]}+C_O.C_N} - (k_4+k_5[\text{cdh1}-\text{APC}]+k_6[\text{p27}])[\text{cyc}-\text{CDK}] \tag{2}$$

$$\frac{d[\text{p27}]}{dt} = k_7 - k_8\frac{C_O.C_N}{K_{[\text{p27}]}+C_O.C_N}[\text{p27}] \tag{3}$$

$$\frac{d[\text{nPRB}]}{dt} = k_9 - (k_{10}+k_9[\text{cyc}-\text{CDK}])[\text{nPRB}] \tag{4}$$

$$\frac{d[\text{p53}]}{dt} = k_{11} - k_{12}\frac{[\text{p27}]}{K_{[\text{p53}]}+[\text{p27}]}[\text{p53}] \tag{5}$$

$$\frac{dR}{dt} = k_{13}R\left(1-\left(\frac{R}{R_*}\right)^3\right) \tag{6}$$

$$\frac{dM}{dt} = k_{14}M\left(1-\frac{M}{M_*}\right) \tag{7}$$

In Equations (1)–(7), [cdh1-APC], [cyclin-CDK], [p27], [nPRB], and [p53] are dimensionless variables whereas R and m are in μm, ng scale. In the above equations, k_1 to k_{14} are the kinetic parameters. k_1 to k_{14}, $K_{[\text{cyc}-\text{CDK}]}$, $K_{[\text{p27}]}$, $K_{[\text{p53}]}$, and α are the dimensionless constants (DC). In (1), J_3 and J_4 are the Michaelis–Menten constants and « 1. In (6) and (7), R_* and M_* represent the radius and mass of an adult proliferative tumour cell. In (2) and (3), C_N and C_O represent the surrounding extracellular nutrients and oxygen levels (dimensionless). Most of the variables in this model are taken from the previous literature, but some of them like, k_2, k_3, k_{11}, k_{13}, k_{14}, α, $K_{[\text{cyc-CDK}]}$, and $K_{[\text{p53}]}$ are very difficult to find out.

Table 1
Parameters value for the system of ODEs.

Parameter	Values for tumour cell	Unit	Reference
k_1	10.0	DC	Alarcón et al. (2004)
k_2	20.0	DC	
k_3	0.03	DC	
k_4	0.40	DC	Alarcón et al. (2004)
k_5	1.0	DC	Alarcón et al. (2004)
k_6	0.25	DC	Alarcón et al. (2004)
k_7	0.007	DC	Alarcón et al. (2004)
k_8	0.01	DC	Alarcón et al. (2004)
k_9	0.01	DC	Alarcón et al. (2004)
k_{10}	0.10	DC	Alarcón et al. (2004)
k_{11}	0.002	DC	
k_{12}	0.01	DC	Perfahl et al. (2011)
k_{13}	0.1	DC	
k_{14}	0.25	DC	
J_3	0.01	DC	Alarcón et al. (2004)
J_4	0.01	DC	Alarcón et al. (2004)
α	0.75	DC	
$K_{[\text{cyc-CDK}]}$	0.01	DC	
$K_{[\text{p27}]}$	0.01	DC	Alarcón et al. (2004)
$K_{[\text{p53}]}$	0.01	DC	
R_*	9.953	μm	Alarcón et al. (2004)
M_*	1.0	ng	https://bionumbers.hms.harvard.edu/

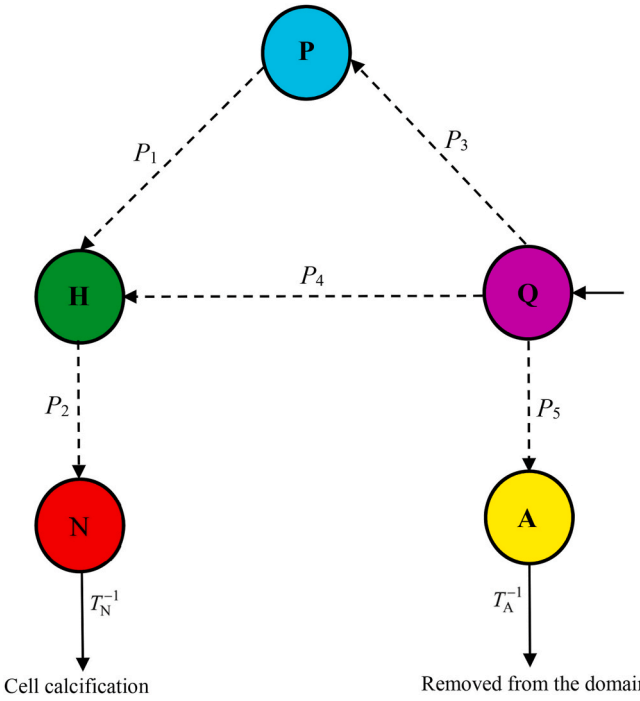

Fig. 5. Phenotypic state transition diagram of tumour cells. Solid lines represent the deterministic transitions whereas the dotted lines indicates the stochastic transitions.

Hence, the values of these parameters are set from the phenomenological arguments. The model considers that, cell division will occur whenever, [cdh1-APC] is below some threshold $[\text{cdh1-APC}]_{th}$ and [cyc-CDK] is above some threshold $[\text{cyc-CDK}]_{th}$. In this research, we consider that, $[\text{cdh1-APC}]_{th} = 0.004$ and $[\text{cyc-CDK}]_{th} = 0.05$ (Alarcón et al. (2004)). The model further assumes that, the cell cycle phase 'G1' lasts until the concentration [cdh1-APC] is higher level than [cyc-CDK], whereas, [cyc-CDK] remains at higher level than [cdh1-APC] during the other phases 'S-G2-M' of cell cycle (Fig. 4 (b)).

The system of Equations (1)–(7) are solved using 4th-order Runge-Kutta method with the parameters value mentioned in Table 1. The solutions of the ODEs are plotted (Fig. 4 (a), (b)) with cell radius (Fig. 4 (c)) and cell mass (Fig. 4 (d)). It is found that, the duration of the cell cycle in this simulation is 23.86 ± 7.76h. The initial conditions to solve the system of ODEs (1) to (7) are as follows (Alarcón et al. (2004)):

$$[\text{cdh1} - \text{APC}]_{t=0} = 0.9;\ [\text{cyc} - \text{Cdk}]_{t=0} = 0.01;\ [\text{p27}]_{t=0} = 0.0;\ [\text{nPRB}]_{t=0} = 1.0;$$

$$[\text{p53}]_{t=0} = 0.0;\ R_{t=0} = \frac{R_*}{2};\ \text{and}\ M_{t=0} = \frac{M_*}{2}$$

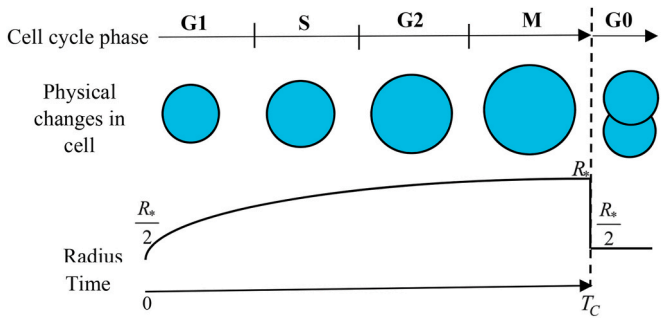

Fig. 6. Proliferation rules.

3. Cellular layer modelling

Cell division is an internal process of a cell but its effects are observed in cellular layer. During cell division, successive number of mutations may change the phenotype of a cell. These mutations have occurred not only due to internal events but also due to the influence of its surrounding neighbourhood, external nutrients, and oxygen levels. Different types of cells communicate with each other and the surrounding microenvironment through several signalling pathways. At cellular layer, cells interact with each other through adhesion protein molecules (E-cadherin) (Panorchan et al., 2006). Adhesion molecule receptors of cell i bind with the ligands of another cell j in *homophilic adhesion* mode which creates an adhesive force among the tumour cells. In this paper, we assume, nutrients act as a chemosensory stimuli for the tumour cells which creates chemotactic force and a drag force by the luminal fluids. These forces act simultaneously and create a resultant force on tumour cells which help to move them in the domain space freely.

The phenotypic changes among cells are described in detail in subsection 3.1 and the forces applied on the tumour cells are discussed in subsection 3.2.

3.1. Phenotypes of tumour cells

A tumour cell in its life time can be one of the phenotypic states in S_T = {'P', 'H', 'Q', 'A', 'N'}. While 'P', 'Q', 'H', 'A', and 'N' are denoting proliferative, hypoxic, quiescent, apoptotic, and necrotic state respectively. The model considers that every tumour cell is in quiescent state initially (default state). Hence, an extra arrow sign in 'Q' (Fig. 5) indicates the default initial state. The colour code used in this Fig. 5 is maintained throughout the research paper to indicate the corresponding phenotype. After that its phenotype change due to internal, as well as surrounding microenvironment. The phenotypic changes have been occurred due to successive mutations. Therefore, phenotypic state (S_T) of a tumour cell at time $t + \Delta t$ depends on the current phenotypic state at t, its internal conditions, and the surrounding microenvironment. The phenotypic state transition diagram of tumour cells are shown in Fig. 5.

3.1.1. Proliferative cells

A proliferative cell remains in 'P' state unless it transforms into other phenotypes ('H') due to surrounding microenvironment or it divides into

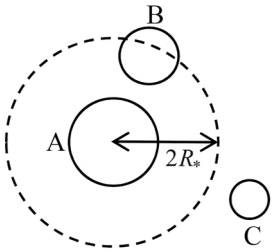

Fig. 7. Neighbourhood rules. Cells which present within the fixed radius (r) of cell A are the neighbouring cells of A. According to the rule, B is the neighbouring cell of A but C is not.

two identical daughter cells with radius $R_*/2$ and mass $M_*/2$ when it becomes mature/adult (Fig. 6). The daughter cells occupy two random positions in the neighbourhood of the parent cell. In the absence of mitogenic stimuli, cell cycle arrest (at 'G0' state) in the early 'G1' phase and becomes quiescent ('Q'). Hence, for the sake of simplicity, in this research, it is considered that, initially the daughter cells are in 'Q' state and its phenotype would be changed depending on the surrounding microenvironment.

The model considers that, there is a chance that a tumour cell transforms from 'P' to 'H', if p27 protein concentration within the cell increases beyond the threshold level $[\mathrm{p27}]^{\mathrm{H}}_{th}$ due to lack of oxygen and nutrients supply. The model considers that the cells in 'H' state are suspend from its cell cycle. The probability P_1 is defined in Equation (8) as,

$$P_1(S_{\mathrm{T}}(t+\Delta t)=^{'}\mathrm{H}^{'}|S_{\mathrm{T}}(t)=^{'}\mathrm{P}^{'})=1-\exp\left(\frac{[\mathrm{p27}]-[\mathrm{p27}]^{\mathrm{H}}_{th}}{[\mathrm{p27}]^{\mathrm{H}}_{th}}\right) \tag{8}$$

An adult proliferative cell spawns two identical daughter cells. These two daughter cell occupy two neighbouring positions randomly. Let, the position of the parent cell be $(x^{'},y^{'})$. The positions of the two daughter cells are defined as (9),

$$\begin{aligned} x_1 &= x^{'}+R_*\cos\phi_1;\ \mathrm{y}_1=y^{'}+R_*\sin\phi_1;\\ x_2 &= x^{'}-R_*\cos\phi_2;\ \mathrm{y}_2=y^{'}-R_*\sin\phi_2; \end{aligned} \tag{9}$$

Where, (x_1, y_1) and (x_2, y_2) are the positions of two daughter cells; ϕ_1, $\phi_2 \in [0, 2\pi)$ with uniform distribution.

3.1.2. Hypoxic cells

The model considers that, probability of a tumour cell in 'H' to be transformed into 'N' state depends on the number of neighbouring cells in hypoxic state (n_{H}), and the time duration (T_{H}) it spend as 'H' phenotype. It is considered that, if n_{H} or T_{H} increases then the chances of transformation from 'H' to 'N' increases. The probability P_2 is defined in Equation (10) as,

$$P_2(S_{\mathrm{T}}(t+\Delta t)=^{'}\mathrm{N}^{'}|S_{\mathrm{T}}(t)=^{'}\mathrm{H}^{'})=1-\exp\left[-\left(\frac{n_{\mathrm{H}}}{1+n_M}\right)\left(\frac{T_{\mathrm{H}}-T_c}{T_c}\right)\right] \tag{10}$$

In this context, the model considers that neighbouring cells of a cell A at time t refers to the cells (Fig. 7) whose centre are lying within a certain fixed distance (r) from the centre of A. Here, we consider.$r = 2R_*$.

3.1.3. Quiescent cells

A quiescent cell can be transformed into either proliferative, or hypoxic, or apoptotic cell. If the surrounding environment is favourable, then a cell in 'Q' state can be transformed into 'P' state with probability P_3. The favourable condition refers to sufficient oxygen ($C_{\mathrm{O}} > \lambda^{\mathrm{P}}_{\mathrm{O}}$) and nutrients ($C_{\mathrm{N}} > \lambda^{\mathrm{P}}_{\mathrm{N}}$). Therefore, the model considers that, the probability P_3 depends on available nutrients and oxygen. The probability P_4 for the transition from 'Q' to 'H' depends on the level of nutrient (C_{N}), oxygen (C_{O}). If the concentration levels reduce below certain levels, *i.e.*, $C_{\mathrm{N}} > \lambda^{\mathrm{Q}}_{\mathrm{N}}$ and $C_{\mathrm{O}} > \lambda^{\mathrm{Q}}_{\mathrm{O}}$, then the possibility

for the transformation from 'Q' to 'H' increase. Further the model assumes that, the probability P_5 for the transition from 'Q' to 'A' depends on the number of neighbouring cells in 'Q' state (n_{Q}), and the duration it spend as 'Q' phenotype (T_{Q}). The probabilities P_3, P_4, and P_5 are defined in Equations 11–13 respectively.

In Equation (11),$\lambda^{\mathrm{P}}_{\mathrm{N}}$ and $\lambda^{\mathrm{P}}_{\mathrm{O}}$ refers to the uptake of nutrients and oxygen by the proliferative cell. In (12), $\lambda^{\mathrm{Q}}_{\mathrm{N}}$ and $\lambda^{\mathrm{Q}}_{\mathrm{O}}$ refers to the uptake of nutrients and oxygen by the quiescent cell respectively.

$$P_3(S_{\mathrm{T}}(t+\Delta t)=^{'}\mathrm{P}^{'}|S_{\mathrm{T}}(t)=^{'}\mathrm{Q}^{'})=1-\exp\left[-\left(\frac{C_{\mathrm{O}}-\lambda^{\mathrm{P}}_{\mathrm{O}}}{\lambda^{\mathrm{P}}_{\mathrm{O}}}\right)\left(\frac{C_{\mathrm{N}}-\lambda^{\mathrm{P}}_{\mathrm{N}}}{\lambda^{\mathrm{P}}_{\mathrm{N}}}\right)\right] \tag{11}$$

$$P_4(S_{\mathrm{T}}(t+\Delta t)=^{'}\mathrm{H}^{'}|S_{\mathrm{T}}(t)=^{'}\mathrm{Q}^{'})=1-\exp\left[-\left(\frac{\lambda^{\mathrm{Q}}_{\mathrm{O}}-C_{\mathrm{O}}}{\lambda^{\mathrm{Q}}_{\mathrm{O}}}\right)\left(\frac{\lambda^{\mathrm{Q}}_{\mathrm{N}}-C_{\mathrm{N}}}{\lambda^{\mathrm{Q}}_{\mathrm{N}}}\right)\right] \tag{12}$$

$$P_5(S_{\mathrm{T}}(t+\Delta t)=^{'}\mathrm{A}^{'}|S_{\mathrm{T}}(t)=^{'}\mathrm{Q}^{'})=1-\exp\left[-\left(\frac{n_{\mathrm{Q}}}{1+n_{\mathrm{M}}}\right)\left(\frac{T_{\mathrm{Q}}-2T_c}{2T_c}\right)\right] \tag{13}$$

In (10) and (13), n_M and T_C refer to the total number of tumour cells present in its neighbourhood and mean cell cycle duration.

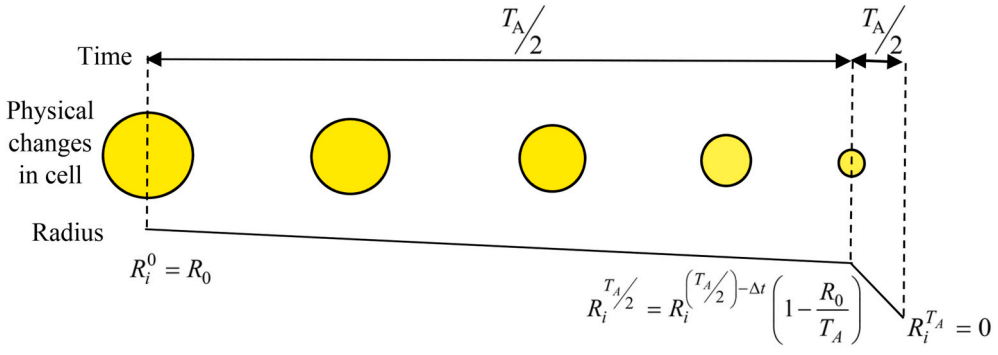

Fig. 8. Apoptosis rules.

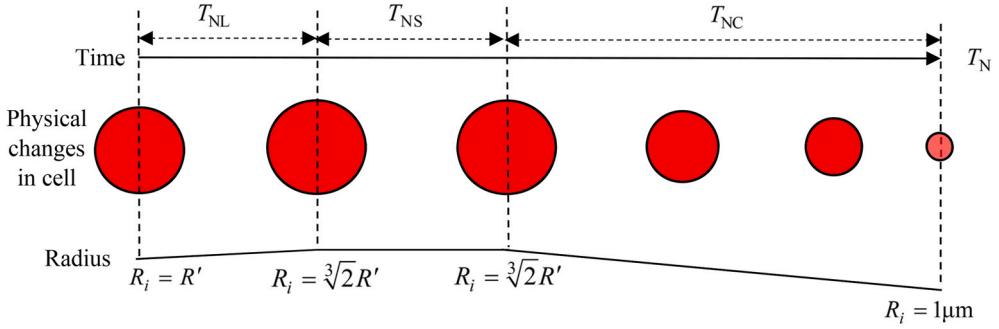

Fig. 9. Calcification process of cell *i*.

Table 2
Parameter values for the simulation of cellular and tissue layer.

Parameter	Value	Unit	Sources
$[p27]^H_{th}$	0.60	DC	
T_c	23.86	h	(from the simulation)
T_A	8.6	h	Macklin et al. (2012); Rocha et al. (2018)
T_N	15.0	Days	Macklin et al. (2012; Rocha et al. (2018)
T_{NL}	6.0	h	Macklin et al. (2012); Rocha et al. (2018)
T_{NS}	18.0	h	Macklin et al. (2012); Rocha et al. (2018)
T_{NC}	14.0	Days	Macklin et al. (2012); Rocha et al. (2018)
λ^P_O	0.1	h^{-1}	Macklin et al. (2012); Rocha et al. (2018)
λ^P_N	0.1	h^{-1}	
λ^Q_O	0.08	h^{-1}	
λ^Q_N	0.08	h^{-1}	
λ^H_O	0.06	h^{-1}	
λ^H_N	0.06	h^{-1}	
λ^{ho}_N	$0.01\lambda^P_N$	h^{-1}	
λ^{ho}_O	$0.01\lambda^P_O$	h^{-1}	Macklin et al. (2012)
λ^b_N	$0.01\lambda^P_N$	h^{-1}	
λ^b_O	$0.01\lambda^P_O$	h^{-1}	Macklin et al. (2012)
η	25κ	$\mu m\ h^{-1}$	Rocha et al. (2018)
κ	100	DC	
D_O	1000	$\mu m^2\ h^{-1}$	Macklin et al. (2012); Rocha et al. (2018)
D_N	900	$\mu m^2\ h^{-1}$	
$^aR^t_i$	$1.214R^t_i$	μm	Macklin et al. (2012); Rocha et al. (2018)

3.1.4. Apoptotic cells

For noncancerous cells, hypoxia is one of the reasons for apoptosis. Whereas, in cancer cells, chances of apoptosis are very less. Apoptosis refers to programmed cell death. Here, it is considered that, after becoming apoptotic, the cell loses its mass and its radius gradually (Equation (14)) up to $T_A/2$ time (Fig. 8). Cells remain in the apoptotic state for a fixed amount of time T_A; afterward they are removed from the domain to model phagocytosis of apoptotic bodies. Their previously-occupied position is made available to the surrounding cells. The algorithm for apoptotic cells is described in Appendix A1.

$$R_i^{T_A/2} = R_i^{\left(T_A/2\right)-\Delta t}\left(1-\frac{R_0}{T_A}\right) \tag{14}$$

3.1.5. Necrotic cells

After being necrotic, tumour cell lose its volume (or radius) and mass not only because of the degradation of surface receptors but also the degradation of their sub-cellular structure. First, the cell swell (up to $\sqrt[3]{2}$ times such that, $R_i \leq R_*$) (Macklin et al., 2012), lyse and loose its fluids. Then the surface receptors become inactive and after that calcification process (Slodkowska et al., 2010; Macklin et al., 2012) has been started. In this paper, we assume that cell mass as well as its radius are reduced at a constant rate and until its radius decreases up to 1 μm. The model considers that the calcification process takes T_N time. Fig. 9 shows the description of calcification process of a necrotic cell.

In this paper, we assume, T_{NL} time is required for cell swelling, lysing, T_{NS} time has taken for inactivation of surface receptors and T_{NC} time is required for the calcification. Therefore, $T_N = T_{NL} + T_{NS} + T_{NC}$. The algorithm for necrotic cell is described in Appendix A2.

All the parameters in Equations 8–13 are dimensionless. The parameter values for simulating the phenotypic transition is summarized in Table 2.

3.2. Tumour cell movement

The model considers that, each tumour cell (i) is characterized by its radius R^t_i, mass m^t_i with a position $\mathbf{X}_i$, velocity $\mathbf{v}_i$, and its phenotype at the time instance t. R^t_i and m^t_i vary with the cell cycle activities (Section 2). The model considers that, tumour cell moves only because of the physical forces apply on it and no phenotypic changes are responsible for the tumour cell motility in avascular phase. We consider that three

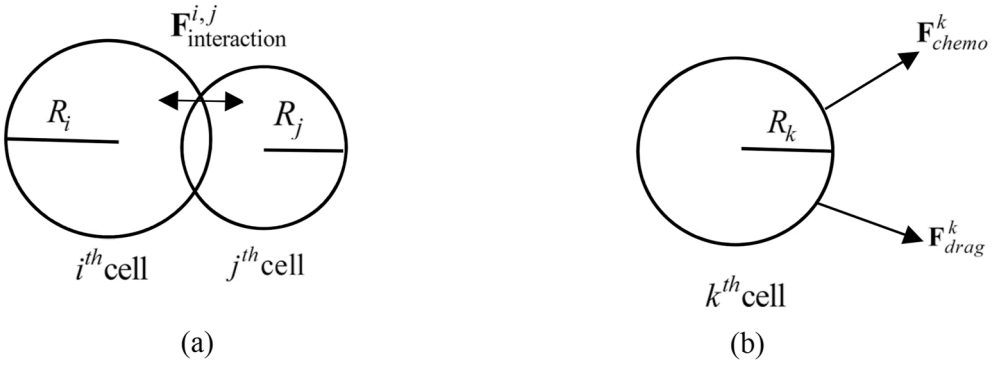

Fig. 10. (a) Shows cell-cell interactive force between two cells and (b) shows the chemotactic, and drag force applied on a cell.

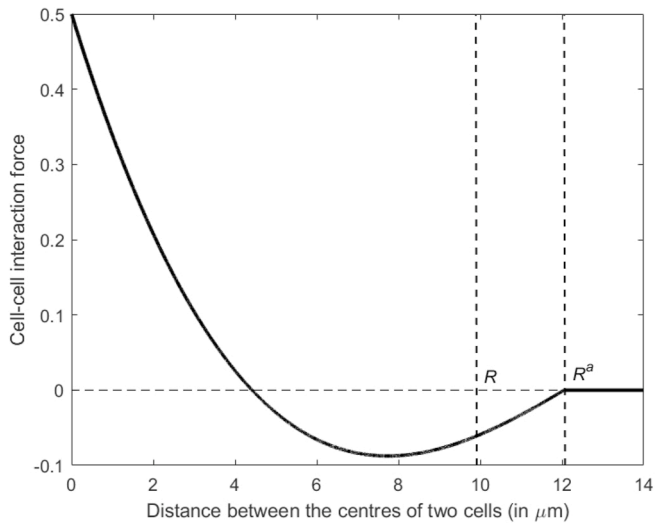

Fig. 11. Cell-cell interaction force for an adult tumour cell.

types of physical forces applied on tumour cell simultaneously: cell-cell interaction force ($\mathbf{F}^{i,j}_{\text{interaction}}$) due to cellular adhesion and repulsion (Fig. 10 (a)); chemotactic force ($\mathbf{F}^{i}_{\text{chemo}}$) due to the gradient of nutrients concentration (Fig. 10 (b)); and drag force ($\mathbf{F}^{i}_{\text{drag}}$) due to luminal fluids (here we ignore any interstitial fluid pressure), that is equivalent to the free flow of water (Wise et al. (2008); Macklin et al. (2012); Rocha et al. (2018)). Therefore, the total physical force applied on a tumour cell i at time instance t is expressed as,

$$\mathbf{F}^i = \underbrace{\mathbf{F}^i_{\text{drag}}}_{\text{drag force}} + \underbrace{\mathbf{F}^i_{\text{chemo}}}_{\text{chemotactic force}} + \sum_{\substack{j=1 \\ j \neq i}}^{B(t)} \underbrace{\mathbf{F}^{i,j}_{\text{interaction}}}_{\text{cell-cell-interaction force}} \tag{15}$$

In Equation (15), $\mathbf{F}^i$ be the total force applied on ith cell and $B(t)$ is the number of cells (dead or alive) present in the domain at the time t.

3.2.1. Cell-cell interaction force

The morphology of a cell changes randomly due to actin polymerization or depolymerisation and it can extend to a sufficiently large distance from the centre of mass of a cell. Throughout the simulation, it is assumed that the tumour cells are circular in shape. We also consider that tumour cell i can be stretched itself beyond its radius (R^t_i) at any time instance t to maintain its adhesive bindings with the surrounding cells. Maximum adhesive interaction distance of a tumour cell is ${}^aR^t_i$ at the time instance t such that, ${}^aR^t_i \geq R^t_i$. In this simulation, we assume, ${}^aR^t_i = 1.214R^t_i$ (Macklin et al. (2012); Rocha et al. (2018)).

In multicellular environment, cellular interaction is an important feature to maintain an equilibrium within the tissue structure. In this model, we consider only cell-cell interaction and ignore cell-matrix, and cell-basement membrane interactions. We also assume that, the

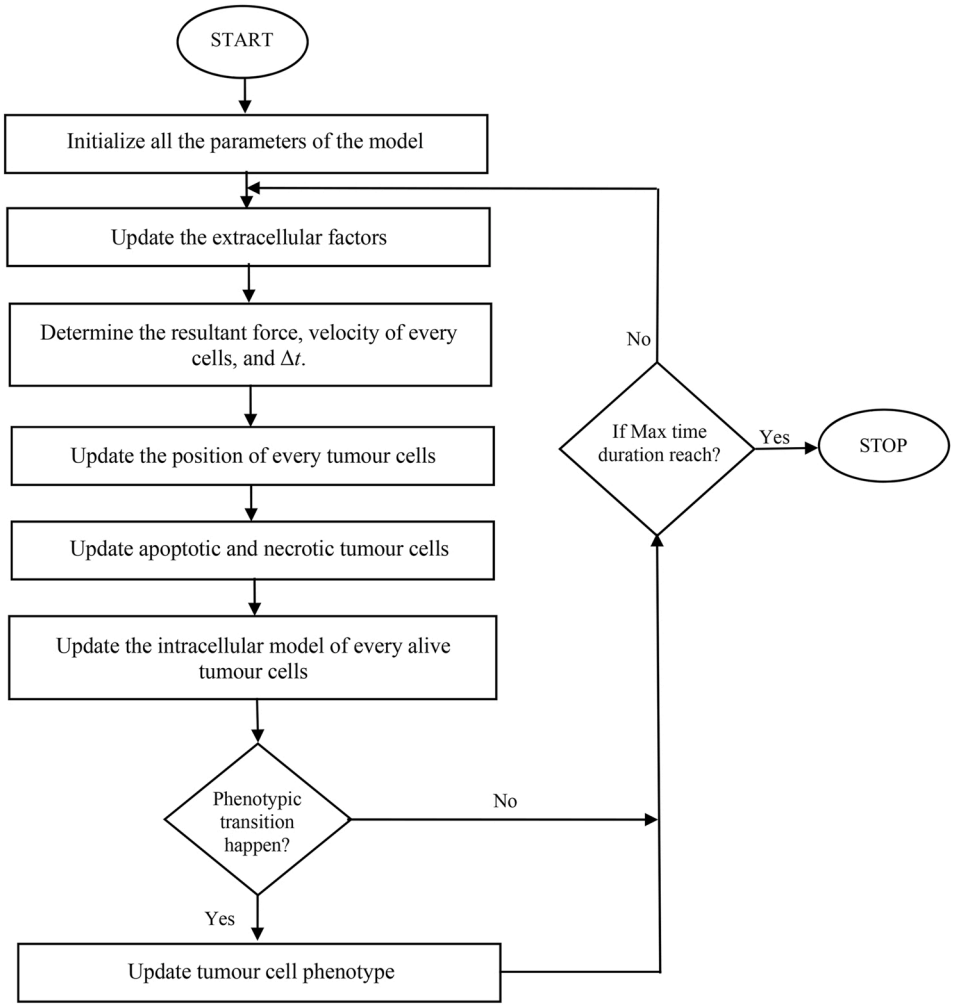

Fig. 12. Flowchart of multi-scale model of avascular tumour growth.

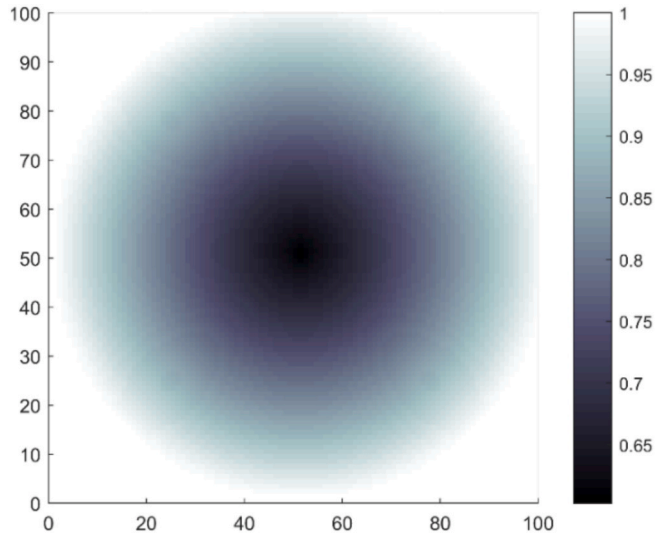

Fig. 13. Initial oxygen distribution for the Experiment 2. (as nutrients distribution also looks same, it is not shown in the figure due to redundancy).

interaction force is applied only by the neighbouring cells of a cell and it helps to control cellular growth, cell division, and cell death (Hansen and Bissell (2000)). Cell-cell interaction force consists of two major components: cell-cell adhesion and cell-cell repulsion. Adhesion force is due to the bonding between adhesion receptors and ligands on the cell's surface (Macklin et al. (2012)). With increment of surface area into direct contact of adjacent cells the adhesion force increases. On the other hand, cells resist compression by the adjacent cells due to cytoskeletons structure, cytoplasm incompressibility, and surface tension of the membranes (Macklin et al. (2012)). Cells' compression resistant is expressed by the repulsion component. Both of these components (adhesion and repulsion) are very weak force.

The governing function (16) to represent the cell-cell interaction force is as follows,

$$\nabla \mathbf{F}^{i,j}_{\text{interaction}}\left(\mathbf{d}, R^t_i a\right) = \begin{cases} -\left(-0.5 + 0.75\left(\frac{|\mathbf{d}|}{R^t_i a}\right)^3 - 2.4\left(\frac{|\mathbf{d}|}{R^t_i a}\right)^2 + 2.15\left(\frac{|\mathbf{d}|}{R^t_i a}\right)\right)\frac{\mathbf{d}}{|\mathbf{d}|} & \text{If } 0 < |\mathbf{d}| \le R^t_i a \\ 0 \qquad \text{Otherwise} \end{cases} \tag{16}$$

Fig. 11 shows that, as the distance between two adjacent cells increase, the adhesion part of the interaction force reduces sharply as the area of contact surface reduces and concurrently the repulsion force increases with the resistance of compression. The repulsion force is zero when two adjacent cells are touching themselves. The interaction force work up to ${}^{a}R^t_i$ distance as we considered previously.

3.2.2. Chemotactic force

Chemotaxis refers the movement of cells towards the higher concentration of chemosensory signals. The model assumes that the nutrients concentration works as chemosensory stimuli and the tumour cells (except the necrotic and apoptotic phenotype) move towards the higher concentration of nutrients. Hence, the chemotactic force is defined as (17),

$$\mathbf{F}^i_{\text{chemo}} = -\eta \nabla C_{\text{N}} \tag{17}$$

where, η is the chemo-sensitivity coefficient.

3.2.3. Drag force

The model assumes that the moving cells experienced a drag force by the luminal fluids. In this context, we neglect the interstitial fluid flow that is equivalent to the free flow of water. Therefore, the drag force is defined as (18),

$$\mathbf{F}^i_{\text{drag}} = -\kappa \mathbf{v}_i \tag{18}$$

where, κ is the constant coefficient (Rocha et al., 2018) and $\mathbf{v}_i$ is the velocity of i^{th} tumour cell. In this context our model ignores the gravitational force.

Newton's second law is applied for balancing the forces applied on cell i (Equation (19)). Similar to Macklin et al. (2012); and Rocha et al. (2018), we make inertialess assumption for this model as the forces are in equilibrium with much smaller time frame than the cell cycle. Therefore, from Equation (15) we get (20),

$$|m_i \dot{\mathbf{v}}_i| = \mathbf{F}^i = \mathbf{F}^i_{\text{drag}} + \mathbf{F}^i_{\text{chemo}} + \sum_{\substack{j=1 \\ j \neq i}}^{B(t)} \mathbf{F}^{i,j}_{\text{interaction}} \tag{19}$$

$$\text{as per our consideration, } |m_i \dot{\mathbf{v}}_i| \approx 0. \text{ Hence, } \mathbf{v}_i = \frac{1}{\kappa}\left[\mathbf{F}^i_{\text{chemo}} + \sum_{\substack{j=1 \\ j \neq i}}^{B(t)} \mathbf{F}^{i,j}_{\text{interaction}}\right] \tag{20}$$

Hence, the position of the ith cell at time instance t is given by, $\mathbf{X}_i(t) = \mathbf{X}_i(t-1) + \mathbf{v}_i \Delta t$, where Δt is the time interval between $t-1$ and t. For the simulation, the parameter values are summarized in Table 2.

4. Tissue layer modelling

To define the tissue layer model, it is considered that $\mathbf{\Phi}$ be an open bounded region in which the target tissue is evolving due to oxygen (C_{O}) and nutrients (C_{N}) from the blood vessels present at the boundary of the region. Let $t \in [0, T]$ be the time duration in which the tissue is evolving.

At the tissue level, the factors of heterogeneous tissues are usually described by a set of scalar fields representing the volume fractions of each factors. The evolution of each factors can be described by the mass conservation equation. In this paper, it is considered that nutrients and oxygen are the only species which diffused from the surrounding blood vessels of a tumour at avascular stage. We assume that, both of the species are soluble substances that spread in the microenvironment through the molecular random walk and very important for nourishment of tumour cells and its growth dynamics. Hence, both the factors are uptaken by the alive cells.

These events in tissue scale are modelled with Fick's law of diffusion equation. In Equation 21 and 22, D_{N} and D_{O} are the diffusion coefficients of nutrients and oxygen respectively. λ_{N} and λ_{O} are (positive constants) uptake coefficients for nutrients and oxygen. λ_{N} and λ_{O} depends on the

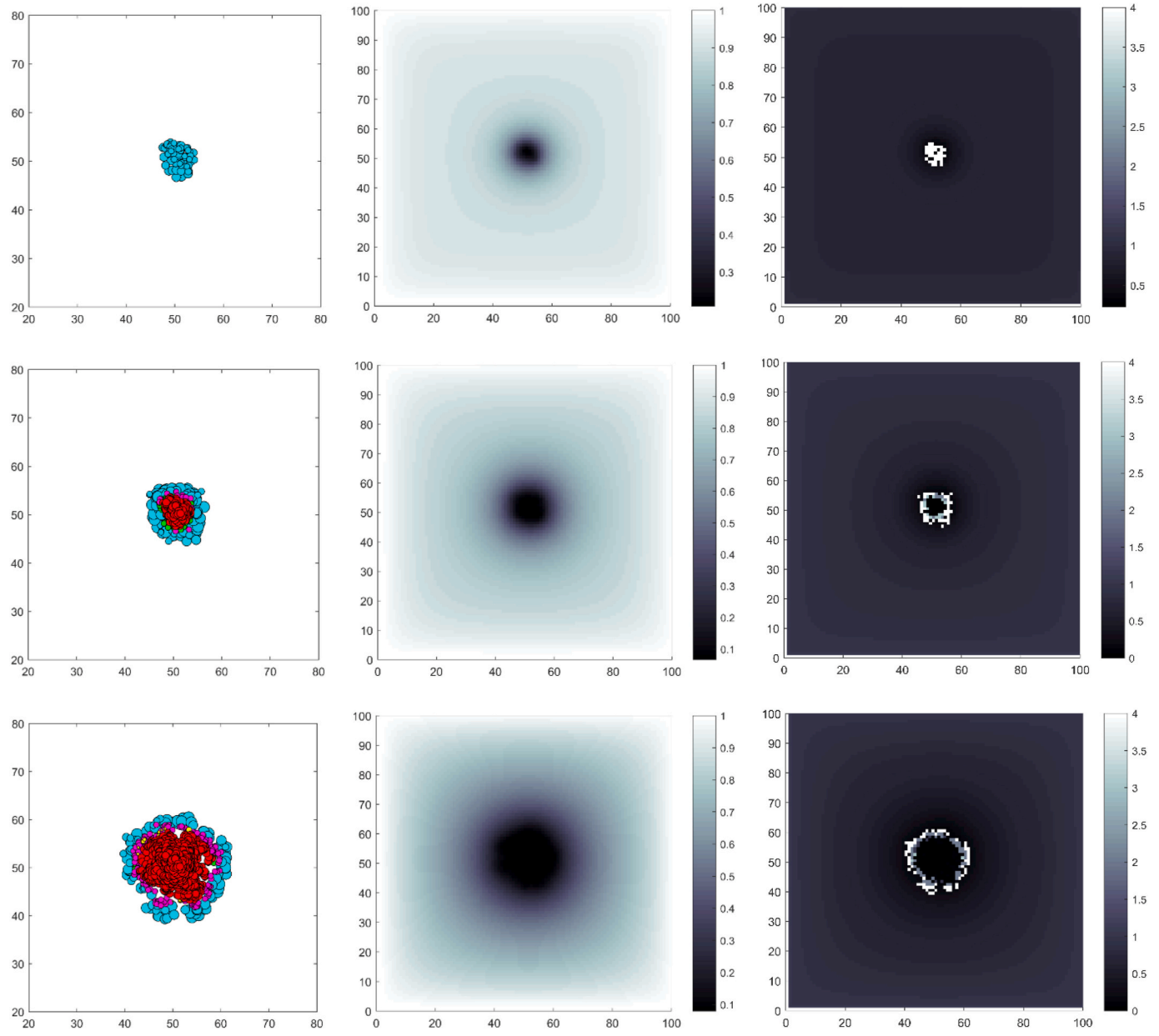

Fig. 14. Simulation result of Experiment 1: Avascular tumour growth dynamics at $t = 100$ h, 200 h, and 400 h. For each time duration the distribution of tumour cells (1st column), oxygen (2nd column) and the distribution of tumour cells and oxygen (nutrients) combined with inverted colour scale (3rd column) are shown. Oxygen and nutrient distribution for every time instances are similar. Hence, only oxygen distribution is shown for different time instances. In tumour cell distribution (1st column) cyan coloured cells represent the proliferative cell, magenta coloured cells represent the quiescent cell, green coloured cell represent the hypoxic cell, yellow coloured cell represents the apoptotic cell, and red coloured cells represent the necrotic cells.

phenotype and the radius of a tumour cell.

$$\frac{\partial C_N}{\partial t} = \nabla.(D_N \nabla C_N) - \lambda_N C_N \tag{21}$$

$$\frac{\partial C_O}{\partial t} = \nabla.(D_O \nabla C_O) - \lambda_O C_O \tag{22}$$

The model considers that, alive tumour cells (proliferative, quiescent, and hypoxic) consume oxygen and nutrients at rates of λ_N^P, λ_N^Q, λ_N^H, λ_O^P, λ_O^Q, and λ_O^H respectively. While host cells uptake oxygen and nutrients at rates of λ_N^{ho}, and λ_O^{ho} and elsewhere oxygen and nutrients decay at a fixed background rate of λ_N^b, and λ_O^b. The model considers that, in a small region Ω around a point (x, y) proliferative cells, quiescent cells, hypoxic cells, host cells, and stroma (non-cells) etc. occupy f_P, f_Q, f_H, f_{ho}, and f_b portions of Ω respectively at time instance t ((Macklin et al., 2012); Hoehme and Drasdo (2010)), where $f_P+f_Q+f_H+f_{ho}+f_b = 1$.

Hence, $\lambda_N(x, y)$ and $\lambda_O(x, y)$ are given by,

$$\lambda_N(x,y) = f_P\lambda_N^P + f_Q\lambda_N^Q + f_H\lambda_N^H + f_{ho}\lambda_N^{ho} + f_b\lambda_N^b \tag{23}$$

$$\lambda_O(x,y) = f_P\lambda_O^P + f_Q\lambda_O^Q + f_H\lambda_O^H + f_{ho}\lambda_O^{ho} + f_b\lambda_O^b \tag{24}$$

Equations 23 and 24 are denoting the weighted uptake rates according to the tissue composition around (x, y). Diffused oxygen and nutrients in the extracellular space are uptaken by the tumour cells at cellular scale. Therefore, the consumptions of oxygen and nutrients are translated from the cellular scale to tissue scale. Here, we transfer the information between these two scales through two nested square grids. Let, H_1 and H_2 are two grids with step size l_1 and l_2; such that $l_2 = l_1/K$, K is any positive and even number. Each node k in H_1 with position (x_k, y_k)

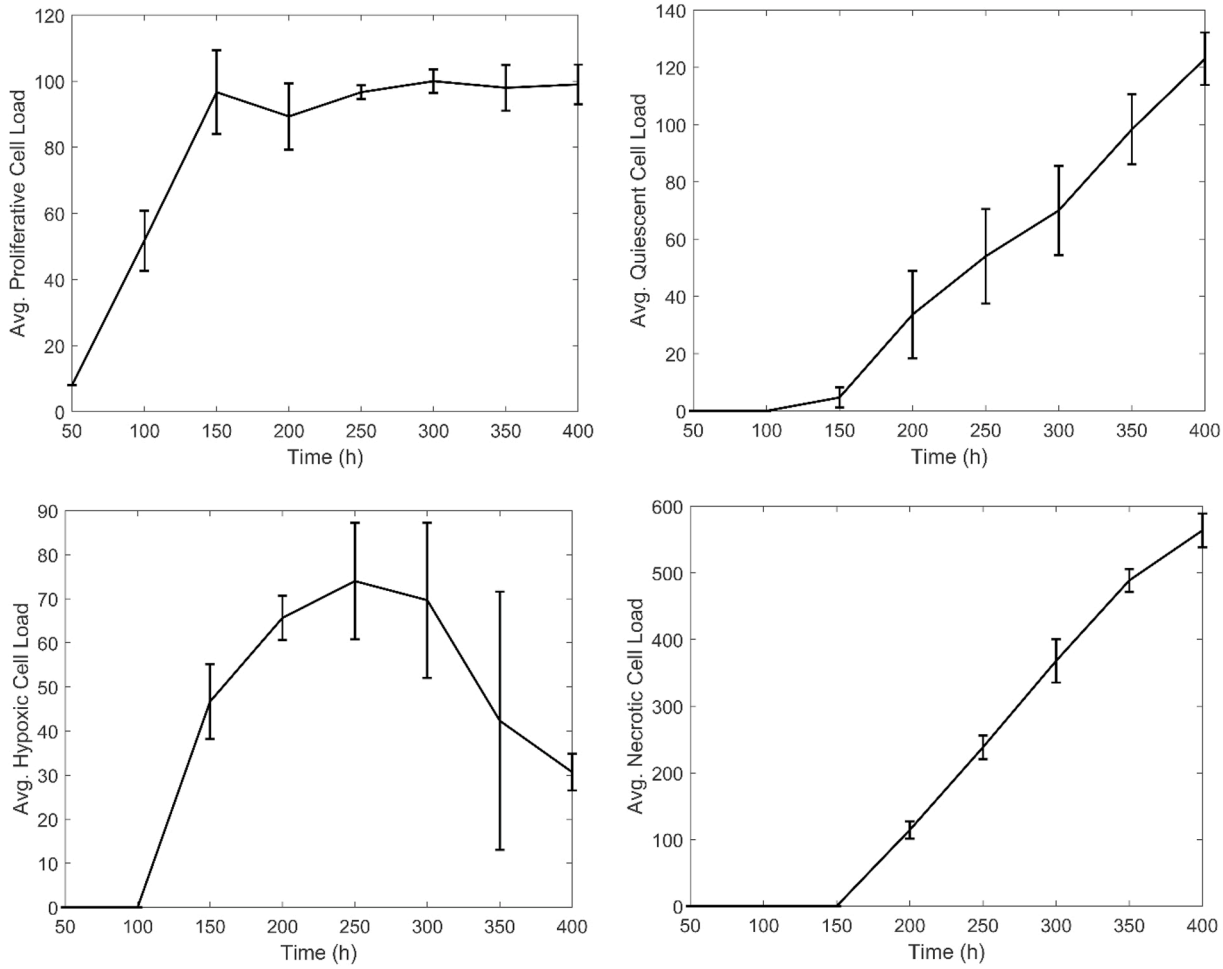

Fig. 15. Different cell loads during the simulations of Experiment 1.

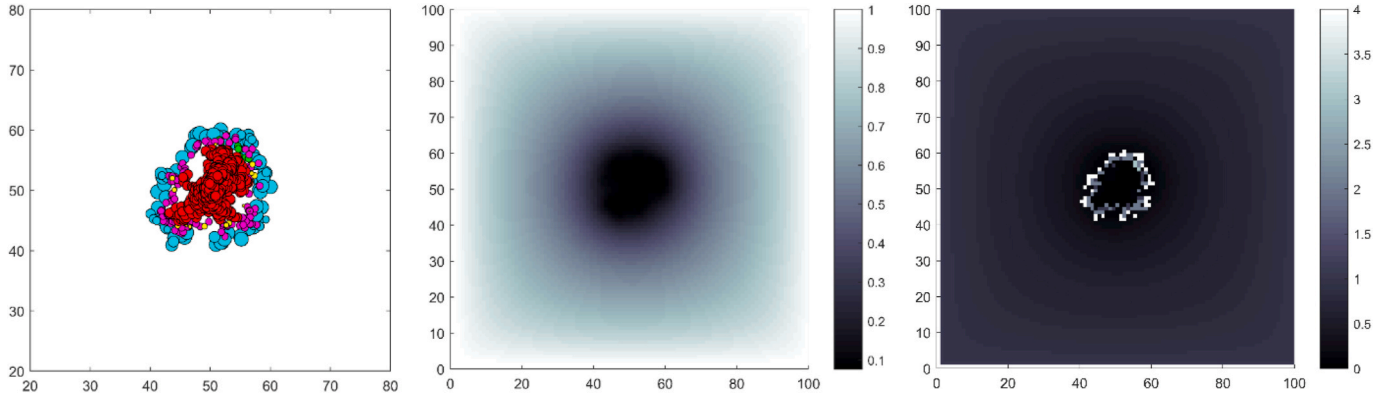

Fig. 16. Simulation result of Experiment 2: Avascular tumour dynamics at $t = 400$ h. The distribution of tumour cells (1st column), oxygen (2nd column) and the distribution of tumour cells and oxygen (nutrients) combined with inverted colour scale (3rd column) are shown. Oxygen and nutrient distribution for every time instances are similar. Hence, only oxygen distribution is shown for the time instance $t = 400$ h. In tumour cell distribution (1st column) cyan coloured cells represent the proliferative cell, magenta coloured cells represent the quiescent cell, green coloured cell represent the hypoxic cell, yellow coloured cell represents the apoptotic cell, and red coloured cells represent the necrotic cells.

is updated with the average value of a square shaped grid in H_2 containing the points (x_p, y_p), such that,

$$|x_p - x_k| < l_2\frac{K}{2},\ |y_p - y_k| < l_2\frac{K}{2}.$$

To exchange the information from the extracellular scale to cellular scale, first we identify the area in H_1 with respect to each point in H_2 and then linearly transfer the values of H_1 into H_2. This mechanism is used to solve the tissue scale model (21), and (22).

5. Computer simulation and results

In this context, a special two dimensional domain of size [0, 1] mm × [0, 1] mm is considered for oxygen and nutrients. Two squared nested

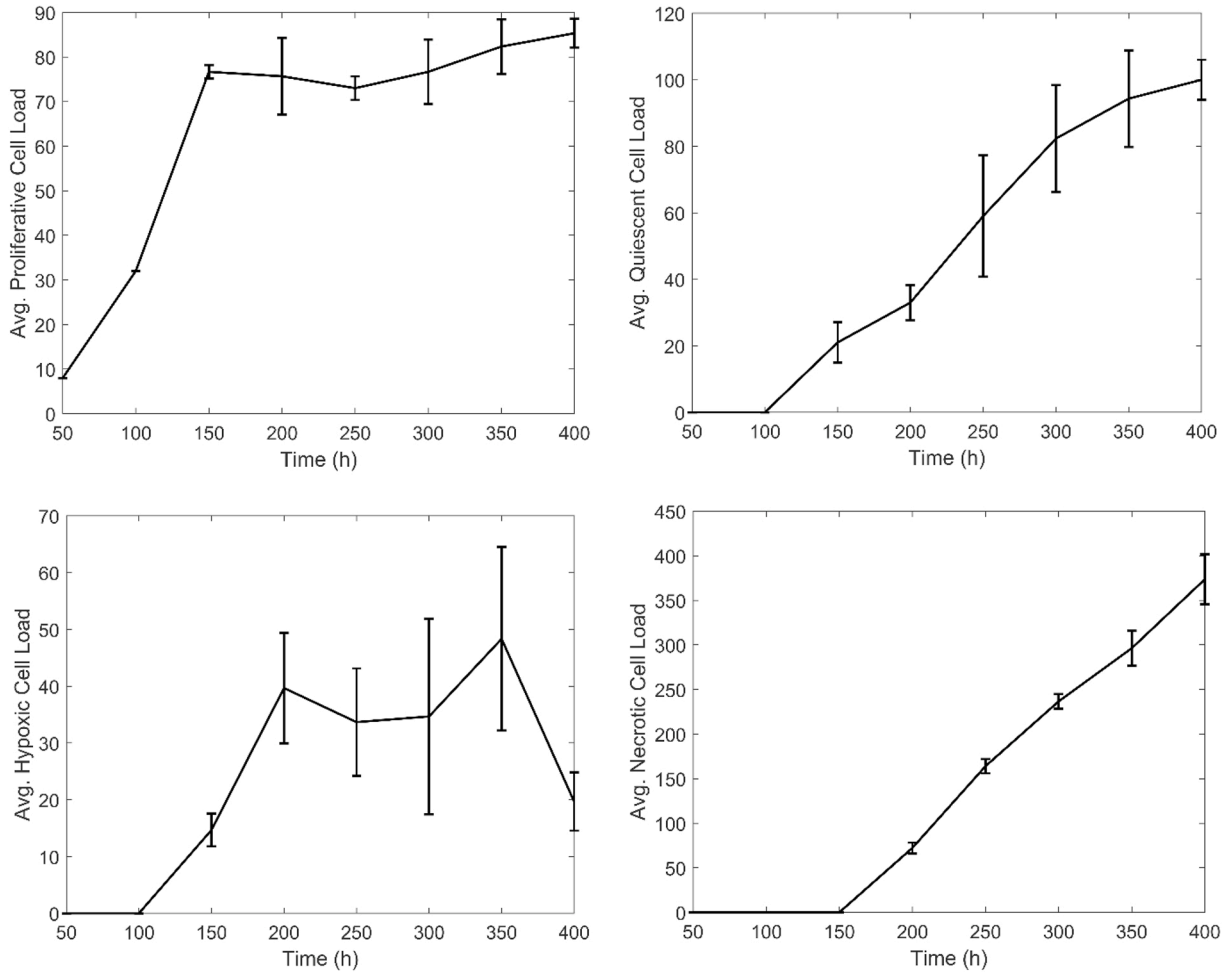

Fig. 17. Different cell loads during the simulation of Experiment 2.

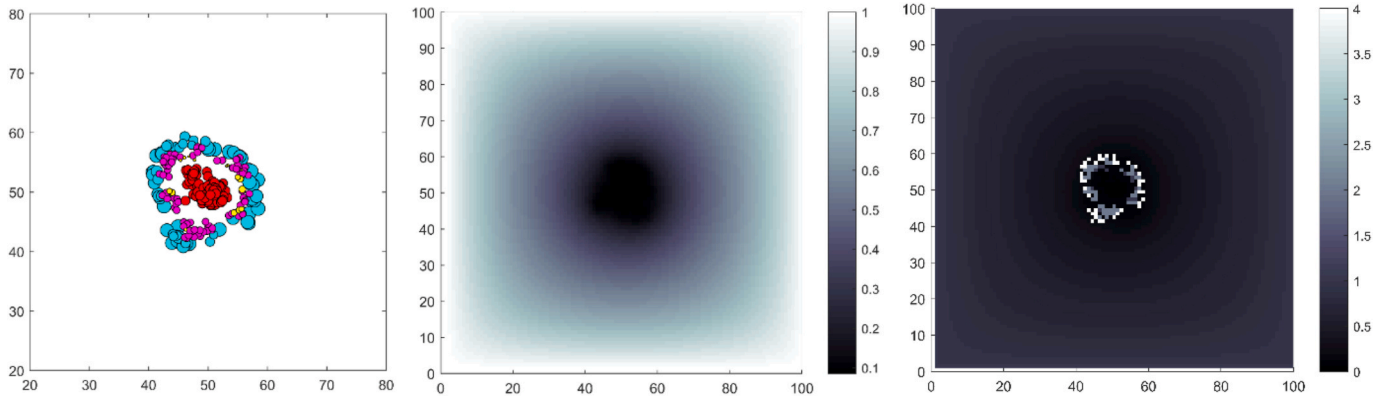

Fig. 18. Simulation result of Experiment 3: Avascular tumour dynamics at $t = 400$ h. The distribution of tumour cells (1st column), oxygen (2nd column) and the distribution of tumour cells and oxygen (nutrients) combined with inverted colour scale (3rd column) are shown. Oxygen and nutrient distribution for every time instances are similar. Hence, only oxygen distribution is shown for the time instance $t = 400$ h. In tumour cell distribution (1st column) cyan coloured cells represent the proliferative cell, magenta coloured cells represent the quiescent cell, green coloured cell represent the hypoxic cell, yellow coloured cell represents the apoptotic cell, and red coloured cells represent the necrotic cells.

grids Z_1 and Z_2 are created to exchange the information of oxygen and nutrients from cellular to extracellular scale. Z_1 consists of 101×101 grid points with the step size $L_1 = 10$ μm (≈radius of an adult tumour cell), while, Z_2 contains 1001×1001 grid points with step size $L_2 = 1$ μm.

The algorithm of this multi-scale model is shown as a flowchart in Fig. 12. After the initialization, the microenvironment of the tumour (oxygen and nutrient concentrations) is updated and translated to every tumour cells. The resultant force on every tumour cells (proliferative, hypoxic, quiescent, apoptotic, and necrotic) are calculated and update the cell velocity with the cell position accordingly. The physical changes related to the dead tumour cells (apoptotic and necrotic) are also

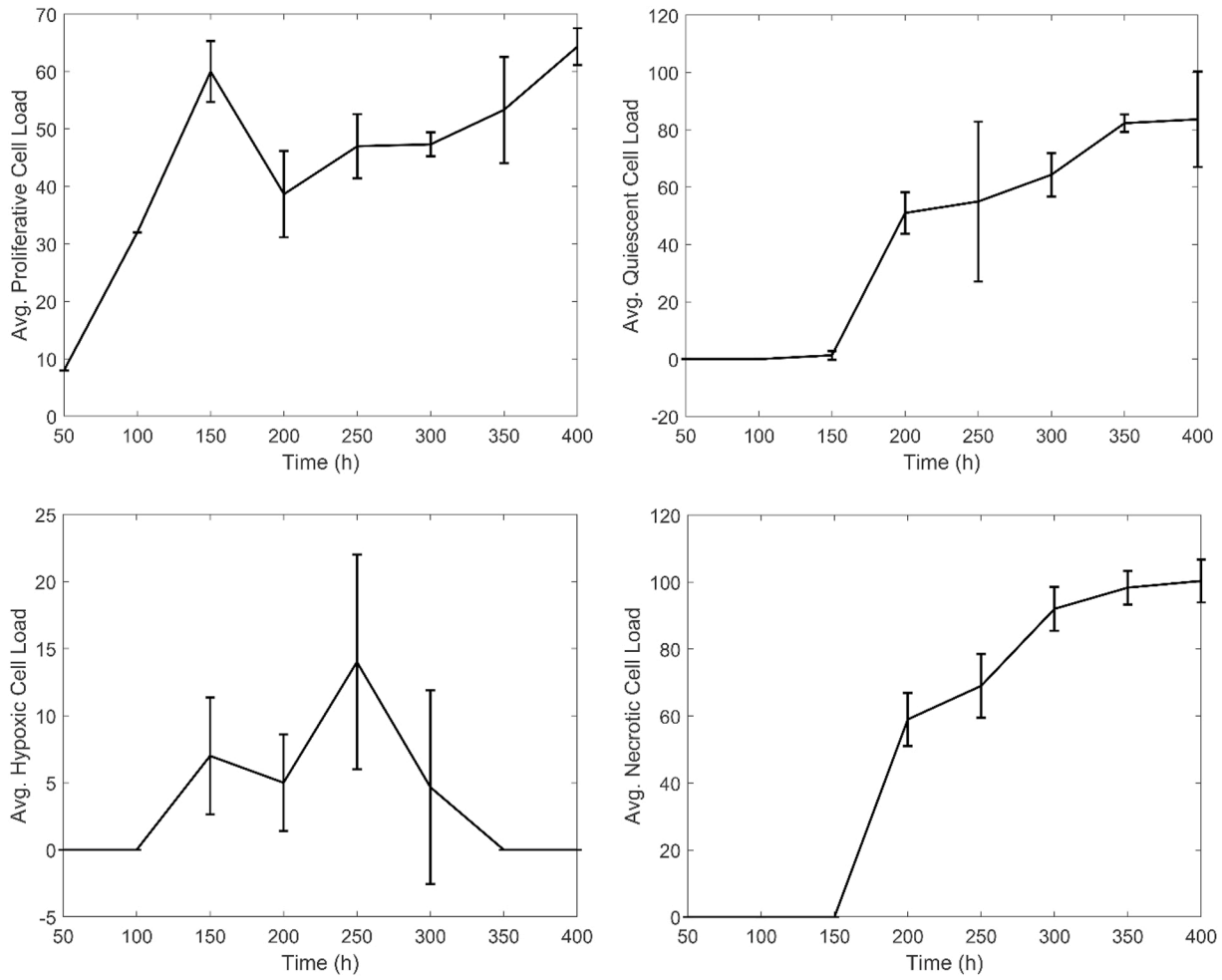

Fig. 19. Different cell loads during the simulations of Experiment 3.

updated simultaneously. The intracellular model for every alive tumour cells are performed by synchronizing with the external factors. This process updates the phenotypic state transition of the alive tumour cells if required. Then, new values of oxygen and nutrients are translated back to the corresponding grid levels. These processes are continued until it reach to the predetermined time period. The algorithm is executed in C++ and all the visualization has been done in MATLAB R2017a.

5.1. Simulation with the base parameters

To verify whether this agent based multi-scale model is able to capture the key characteristics of an avascular tumour growth, the algorithm is simulated with the base parameters mentioned in Tables 1 and 2. Most of these values are taken from the literatures, but some of the parameters are very difficult to find out. So, we set these values from phenomenological arguments. We observe the behaviour of the model in different microenvironments. Particularly, we investigate the roles of oxygen and nutrients in the tumour cell dynamics. Therefore, we have performed three experiments with three different initial distributions of oxygen, and nutrients. The descriptions are as follows.

Experiment 1. Homogeneous microenvironment ($C_O[i, j] = 1.0$, $C_N[i, j] = 1.0$ at $t = 0$ for all i, j).

Experiment 2. Heterogeneous microenvironment ($0 \leq C_O[i, j] \leq 1.0$, $0 \leq C_N[i, j] \leq 1.0$ at $t = 0$ for all i, j), where $C_O[i, j]$ and $C_N[i, j]$ are generated from a mathematical function that is a combination of Euclidian distance and decay function (Fig. 13).

Experiment 3. Random microenvironment ($0 \leq C_O[i, j] \leq 1.0$, $0 \leq C_N[i, j] \leq 1.0$ at $t = 0$ for all i, j).

We also test (under homogeneous microenvironment) this model by modifying few assumptions with some varying simulation parameters within biologically realistic ranges. Our aim is to ensure that the model produces realistic outcome and helps us to gain insight into the underlying biology. All the experiments are performed three times, and each time two proliferative cells are placed at the centre of a square domain initially. For each studies we have taken the average results. This way, we have studied the effect of chemotaxis on tumour growth dynamics as well as on the count of different phenotypes. We also investigate the roles of p27 proteins on tumour growth and its dynamics.

Fig. 14 shows one of the simulation results (among three simulations) for the Experiment 1. The experiment begins ($t = 0$) with two proliferative cells are placed at the centre of a uniformly distributed oxygen and nutrients domain. The tumour is developed by absorbing the surrounding oxygen and nutrients. At $t = 100$ h, the tumour nodule is composed of proliferative cells only; other phenotypes are not present during the early stage of simulation. Due to over metabolism of tumour cells, oxygen and nutrients are gradually decreasing at the innermost region of the tumour nodule (Carmeliet and Jain (2000)). At $t = 200$ h, a necrotic core begins to develop at the centre of the tumour. A belt of quiescent cells are also observed around the necrotic core. The proliferative cells are visible at the outer region of the nodule; *i.e.*, a three layer phenotype pattern is formed (Sutherland et al., 1971). At $t = 400$ h, oxygen and nutrients at the centre of the tumour reduce sharply. With the simulation time, the avascular tumour nodule and the necrotic core at the centre of the tumour expand rapidly.

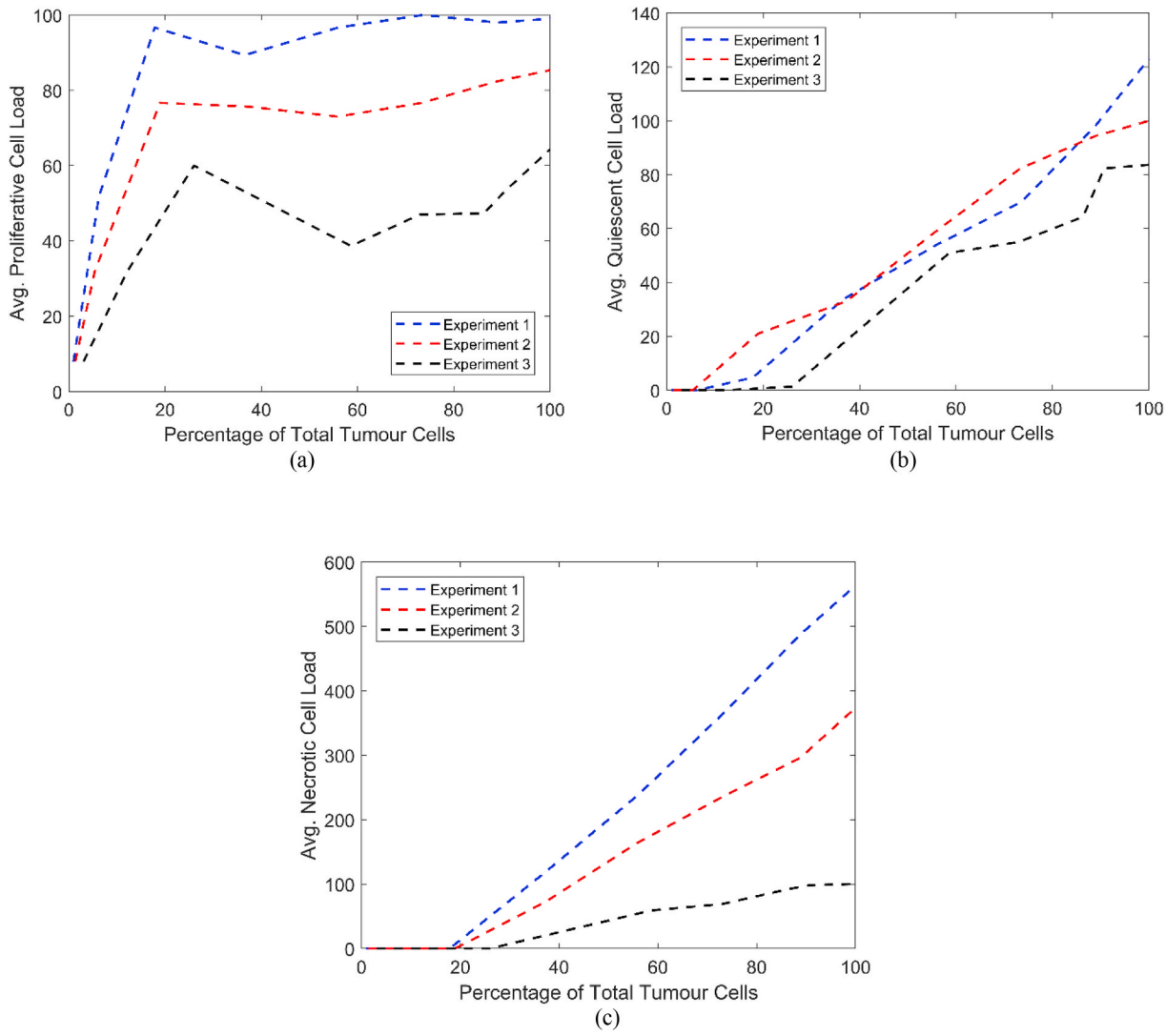

Fig. 20. (a) Avg. proliferative cell load, (b) avg. quiescent cell load, and (c) avg. necrotic cell load with respect to percentage of total tumour cells in Experiment 1, 2, and 3.

The count of different phenotypes of tumour nodule during the simulation of Experiment 1 is plotted in Fig. 15. The figure shows, up to $t = 100$ h of simulation time only proliferative cells are present in the computing domain. After that, quiescent and hypoxic cells come into picture, and after around 150 h of simulation time, necrotic cells are developed. After 150 h of simulation, the nature of the plot of proliferative cells becomes flat, while the quiescent and necrotic cells increase gradually. As the necrotic cells increase rapidly with the simulation time, the growth rate of quiescent cells is not much higher and hypoxic cells decreases after a certain duration (250 h of simulation).

The Experiment 1 (Fig. 14) is performed in a homogeneous environment, so, it is not too surprising that, this has produced almost a symmetric tumour (geometrically). The tumour cell distributions in Experiment 2 (Fig. 16) are almost radically same (symmetric) like the previous one. Therefore, almost similar (like Fig. 15) kind of patterns can be seen in Fig. 17. Whereas, output of Experiment 3 (Fig. 18) is not radially symmetric (cell loads of final tumour are shown in Fig. 19), although, the basic structures (necrotic cells at the centre, quiescent is covering the necrotic, and proliferative cell at the surface of the tumour) of the avascular tumour is maintained for all the three experiments.

When looking at the individual phenotype patterns with respect to total tumour cells in all the experiments, we found that, with the increase in total tumour cells, proliferative cells increase initially. However, after a certain hike in total tumour cells (around 20 percent), the proliferative cells increase marginally in all the three cases (Fig. 20 (a)). On the other hand, quiescent and necrotic cells both increase sharply with the total tumour cells (Fig. 20 (b), (c)), which indicate that with the expansion of tumour mass necrotic cells as well as quiescent cells both increase. Another important observation from Fig. 20 (a)–(c) is that, different cell loads in Experiment 3 are quiet low with respect to Experiment 1, and 2.

Further, we are looking at the individual phenotype, and total tumour cell load patterns with respect to necrotic cells in all the experiments. Same kind of patterns can be observed like Fig. 20 (a)–(c) for proliferative (Fig. 21 (a)), quiescent (Fig. 21 (b)), and total tumour cells (Fig. 21 (c)). These similarities specify that there must be a proportionate relation exist between total tumour cells and necrotic cells.

5.1.1. *The role of chemotaxis in tumour growth dynamics*

To investigate the role of chemotaxis in the homogenous microenvironment, we make $\mathbf{F}_{\text{chemo}} = 0$, for all tumour cells. We observe no interesting pattern in proliferative, quiescent, necrotic and total tumour cell counts in both the cases (Fig. 22 (a) – (d)). However, 'without chemotaxis' ($\mathbf{F}_{\text{chemo}} = 0$), the model always produces less number of cells in all the categories except quiescent cell.

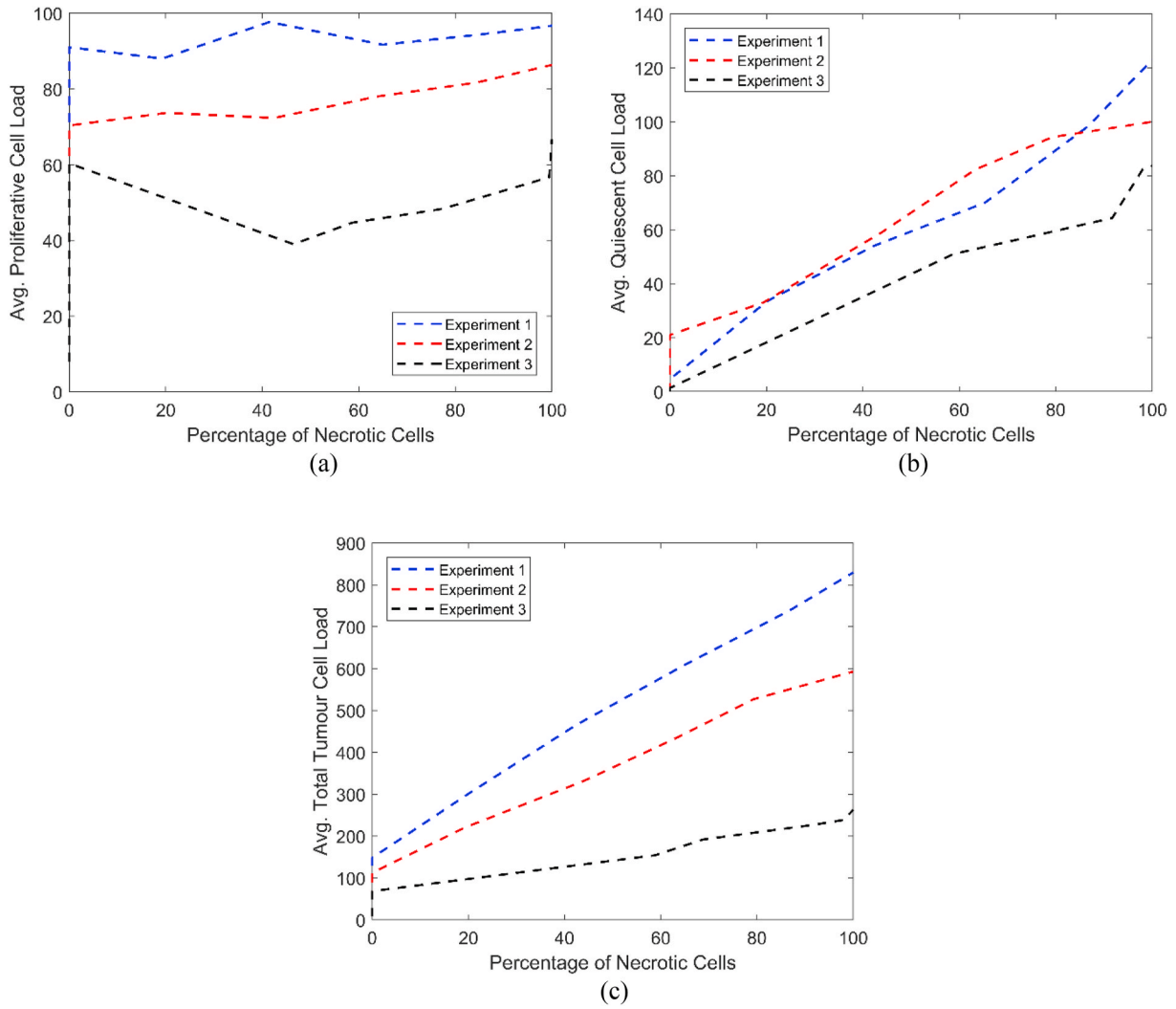

Fig. 21. (a) Avg. proliferative cell load, (b) avg. quiescent cell load, and (c) avg. total tumour cell load with respect to percentage of necrotic cells in Experiment 1, 2, and 3.

5.1.2. The role of p27 in tumour growth dynamics

To examine the role of p27 on tumour growth dynamics, we vary the threshold of p27 from 0.3 to 0.7 with the interval of 0.1 and perform the simulation in homogeneous microenvironment. We observe that (Fig. 23), with the increasing threshold value of p27, loads of proliferative cells are not much varying. The quiescent cell loads in the final tumour are decreasing from the threshold value of 0.5 though a slight uptrend is observed at 0.5. On the other hand, cell loads in necrotic and total tumour cells in final cell load are looking very similar with varying the threshold of p27. Both initially decrease up to 0.4, and then a certain up trends are visible in both the cases up to 0.5 and then another fall is observed up to 0.6 and then another uptrend is visible up to 0.7.

6. Discussions and conclusions

In this paper, we have developed a multi-scale agent based hybrid framework for avascular tumour growth in two dimensions. In this modelling approach we consider every tumour cell as a cellular agent which reacts on its internal proteins as well as surrounding microenvironment (surrounding cells, oxygen, and nutrients). The proliferative cellular agents grow, spawn two identical daughter agents, or it may transform into different phenotypes. The model also considers the biophysical forces due to cell-cell interaction, chemotaxis due to diffused nutrients and a drag force due to luminal fluids.

At the early stage, tumour nodule looks like small sized cellular mass and it is rarely seen clinically. Sutherland and his lab mates had studied the multicellular spheroid *in vitro* extensively (Sutherland et al., 1971; Sutherland (1988)) to identify the underlying internal properties for developing therapeutic strategies. The multicellular spheroid has a well-established structure: its centre contains a necrotic core of dead cells that covers most of the area in tumour spheroid (in 2-D). The necrotic core is surrounded by a rim of quiescent cells, which are alive but cannot divide, and the proliferative cells lie in the outer region of the spheroid. In carrying out the computational simulations, we found that this modelling framework offers biologically realistic outcomes (Figs. 14 and 16–18) as described by (Sutherland et al., 1971; Sutherland (1988)).

Further, we validate this model with immunohistochemistry and histopathology data of an anonymised patient of the M. D. Anderson Cancer Centre (case no. 100019) described in Edgerton et al. (2011), and Macklin et al. (2012). Edgerton et al. (2011) have used a nonlinear continuum model developed by Cristini et al. (2003) for patient specific prediction of tumour volumes of ductal carcinoma *in situ* (DCIS) based on histological image measurements. This prediction is very much crucial for more accurately determine the size for complete tumour excision. Edgerton et al. (2011) analysed the patient specific parameters and fit into the model to find the final volume. Macklin et al. (2012) have developed a lattice-free, agent based two layer (cellular and extracellular) model for DCIS. In this model they have employed cell-cell and

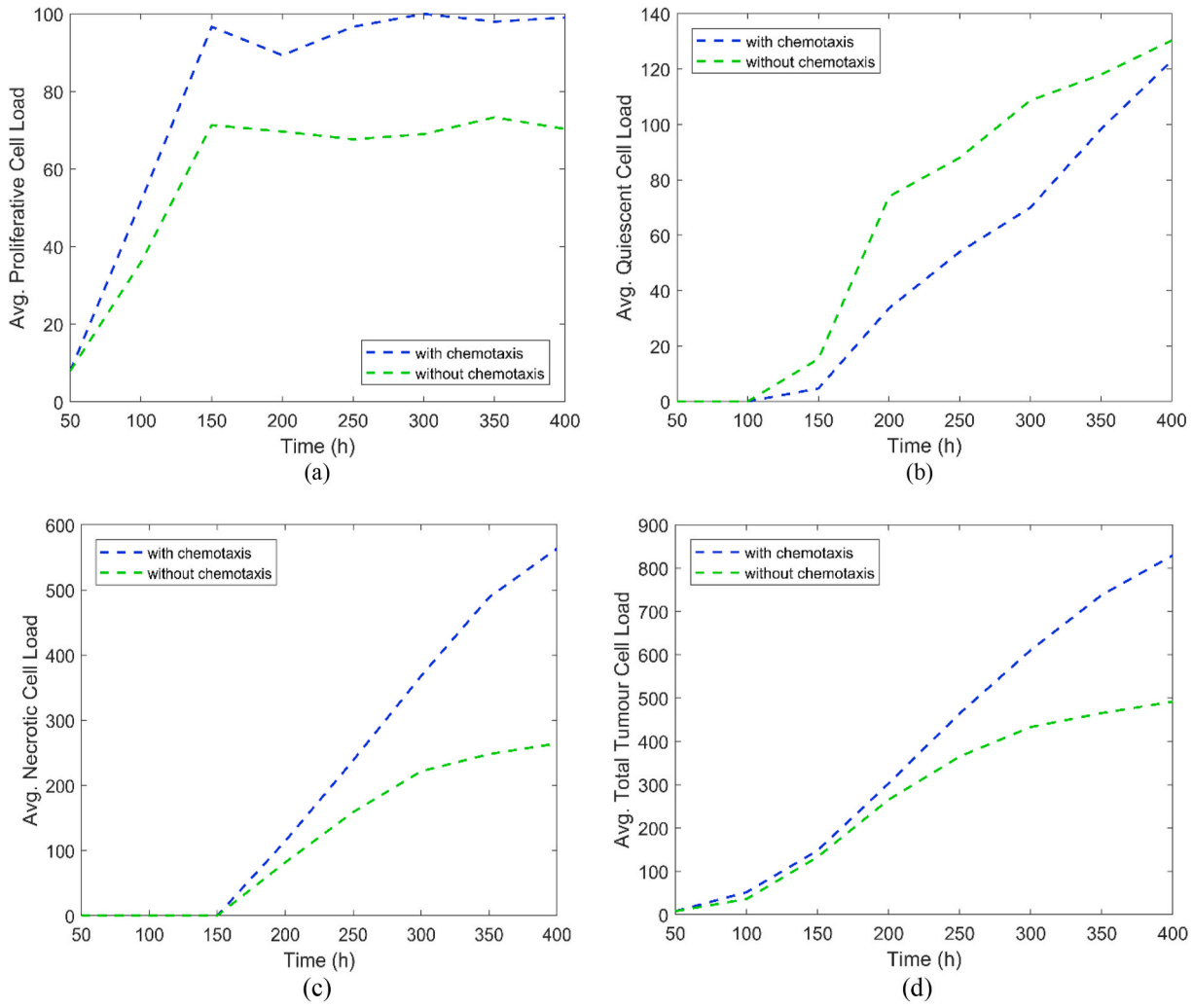

Fig. 22. (a) Avg. proliferative cell load, (b) avg. quiescent cell load, (c) avg. necrotic cell load, and (d) avg. total tumour cell load in homogenous microenvironment with or without chemotaxis.

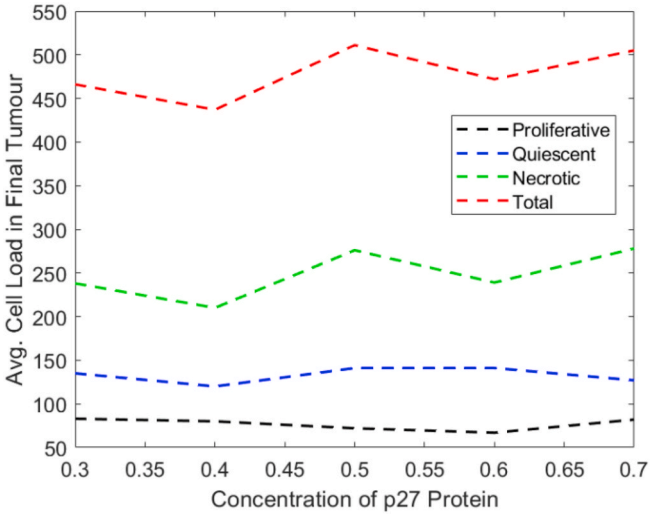

Fig. 23. Avg. proliferative, quiescent, necrotic and total tumour cell load in the final tumour that grows in homogenous microenvironment for different threshold levels of p27.

Table 3
Comparison of patient record (2nd column) and computational (3rd column) results for proliferative index, raw apoptotic index, corrected apoptotic index, viable rim thickness, cell densities, and duct radius.

Quantity	Patient Data	Simulated Data
PI (%)	17.43 ± 9.25	11.3598 ± 1.2259
Raw AI (%)	0.638 ± 0.424	0.4907 ± 0.3261
Corrected AI (%)	0.831 ± 0.572	1.2367 ± 0.5531
Cell density (cells/μm^2)	$0.003213 \pm 5.95 \exp(-4)$	$0.0012 \pm 3.0730 \exp(-5)$
Viable rim thickness (μm)	76.92 ± 12.51	24.7696 ± 4.2154
Duct radius (μm)	170.11 ± 76.37	62.4774 ± 8.4506

cell-basement membrane interactions that are modelled with potential functions. Macklin et al. (2012) have ignored the activities in intracellular layer and also considered fixed cell cycle duration.

In the above literature, the described patient contains a nuclear grade III, mixed cribriform/solid-type DCIS with comedonecrosis. The measurement techniques of these data are described in detail in Edgerton et al. (2011). For validation purpose, we have chosen few parameters like proliferation index (PI), raw apoptotic index (AI), corrected AI, cell density, avg. viable rim thickness, and avg. duct radius. PI refers to the percentage of the ratio of proliferative cells and total tumour cell

quantity (Edgerton et al., 2011); raw AI refers to the percentage of the ratio of apoptotic cells and total tumour cell quantity (Edgerton et al., 2011); corrected AI is found by multiplying the raw AI with (8.6/6.6) (Macklin et al., 2012); cell density refers to the number of tumour cells per μm^2 area; viable rim thickness defines the area of the rim present outside of the tumour that only contains proliferative and quiescent cells; avg. duct radius defines in this case the radius of the tumour spheroid (Macklin et al., 2012).

To validate the model, we simulate our model for 720 h and compute PI, raw AI, cell density, and viable rim thickness at an interval of 1 h after completion of the simulation time for 300 h. As the apoptosis is very rare event in tumour growth with small number of cells (Macklin et al., 2012), therefore, we compute the parameters from 300 h of simulation time. The patient data and simulation data are listed in Table 3. From the data (in Table 3) it can be concluded that, the proposed model is very close to the range of patient data though for measuring cell density, viable rim thickness, and duct radius the model underestimate the data.

The proposed model also covers important criteria of the hallmarks of cancer which include oxygen and nutrients consumption, micro-environmental heterogeneity, tumour cell proliferation by avoiding growth suppressor signals and replicating at an abnormally faster rate, and resistance of apoptosis (Hanahan and Weinberg (2000); Hanahan and Weinberg (2011)). However, there is a scope for the improvement to correctly predict the patient data. As, we model individual cell dynamics, our framework can be easily extended to develop a model for tumour induced angiogenesis which involves development of vascular network from the pre-existing local vessels due to tumour angiogenic factors diffused from hypoxic tumour cells. Further, the framework may be used to study tumour invasive growth and metastasis.

Declaration of competing interest

On behalf of all authors, the corresponding author states that there is no conflict of interest.

Acknowledgement

We would like to thank Dr. Abir Igamberdiev, Editor-in-Chief of BioSystems for being supportive towards the publication of this paper. We show our sincere gratitude to the anonymous reviewer(s) whose valuable comments helped us greatly to improve the presentation. Also, the first author of this paper is thankful to the University Grant Commission, Government of India for supporting him with a Senior Research Fellowship.

Appendix A1. Algorithm for apoptotic cell

Input : i, R_i^0, m_i^0, T_A

$//R_i^0$ and m_i^0 be the radius and mass of i^{th} cell at $t = 0$

$//T_A$ be the time duration of an apoptotic cell present at the computational domain

Step1: $t \leftarrow 0$;

Step2: While $t + \Delta t \leq \frac{T_A}{2}$

$R_i^{t+\Delta t} \leftarrow R_i^t \left(1 - \frac{R_i^0}{T_A}\right)$;

$m_i^{t+\Delta t} \leftarrow m_i^0 \left(\frac{R_i^{t+\Delta t}}{R_i^0}\right)$;

End While

Step3: While $t + \Delta t > \frac{T_A}{2} \& t + \Delta t < T_A$

Do nothing;

End While

Step4: If $t + \Delta t == T_A$

Apoptotic cell is removed from the computational domain;

End If

Appendix A2. Algorithm for the necrotic cells

Input : $i, R_i^t, m_i^t, T_{NL}, T_{NS}, T_{NC}$

$//R_i^t$be the radius and mass of i^{th} cell at time instance t

$//T_{NL}$ be the time duration of a necrotic cell swelling

$//T_{NS}$ be the time duration of inactivation of surface receptors

$//T_{NC}$ be the time duration of calcification

Step1: If $\sqrt[3]{2}R_i^t \leq R_*$

$swelling\ rate \leftarrow \left(\sqrt[3]{2}R_i^t - R_i^t\right)/T_{NL}$;

$mass\ increase\ rate \leftarrow \left(\sqrt[3]{2}m_i^t - m_i^t\right)/T_{NL}$;

Else

$swelling\ rate \leftarrow \left(R_* - R_i^t\right)/T_{NL}$;

$mass\ increase\ rate \leftarrow \left(m_* - m_i^t\right)/T_{NL}$;

End If

Step2: While $t + \Delta t \leq T_{NL}$

$R_i^t \leftarrow R_i^t + swelling\ rate^*\Delta t$;

$m_i^t \leftarrow m_i^t + mass\ increase\ rate^*\Delta t$;

End While

Step3: While $t + \Delta t > T_{NL} \& t + \Delta t \leq T_{NS} + T_{NL}$

Inactivation of surface receptors;

End While

Step4: While $t + \Delta t > T_{NS} + T_{NL} \& t + \Delta t \leq T_{NS} + T_{NL} + T_{NC}$

$m_i^t \leftarrow m_i^t - \left(m_i^t/R_i^t\right)$;

$R_i^t \leftarrow R_i^t - \left(R_i^t - 1\right)/T_{NC}$;

End While

Step5: While $t + \Delta t > T_{NS} + T_{NL} + T_{NC}$

Do nothing;

End While;

References

Alarcón, T., Byrne, H.M., Maini, P.K., 2004. A mathematical model of the effects of hypoxia on the cell-cycle of normal and cancer cells. J. Theor. Biol. 229 (3), 395–411.

Bionumbers, 20th July, 2020. https://bionumbers.hms.harvard.edu/.

Carmeliet, P., Jain, R.K., 2000. Angiogenesis in cancer and other diseases. Nature 407 (6801), 249–257.

Chaplain, M.A., Powathil, G.G., 2016. Multiscale modelling of Cancer progression and treatment control: the role of intracellular heterogeneities in chemotherapy treatment. In: Research on the Physics of Cancer: A Global Perspective, pp. 1–18.

Choi, H.R., Tucker, S.A., Huang, Z., Gillenwater, A.M., Luna, M.A., Batsakis, J.G., El-Naggar, A.K., 2003. Differential expressions of cyclin-dependent kinase inhibitors (p27 and p21) and their relation to p53 and Ki-67 in oral squamous tumorigenesis. Int. J. Oncol. 22 (2), 409–414.

Clyde, R.G., Bown, J.L., Hupp, T.R., Zhelev, N., Crawford, J.W., 2006. The role of modelling in identifying drug targets for diseases of the cell cycle. J. R. Soc. Interface 3 (10), 617–627.

Cristini, V., Lowengrub, J., Nie, Q., 2003. Nonlinear simulation of tumor growth. J. Math. Biol. 46 (3), 191–224.
Edgerton, M.E., Chuang, Y.L., Macklin, P., Yang, W., Bearer, E.L., Cristini, V., 2011. A novel, patient-specific mathematical pathology approach for assessment of surgical volume: application to ductal carcinoma in situ of the breast. Analytical cellular pathology 34 (5), 247–263.
Folkman, J., 1974. Tumor Angiogenesis. In: Advances in Cancer Research, vol. 19. Academic Press, pp. 331–358.
Folkman, J., 1976. The vascularization of tumors. Sci. Am. 234 (5), 58–73.
Folkman, J., 1985. Tumor angiogenesis. Adv. Canc. Res. 43, 175–203.
Folkman, J., Klagsbrun, M., 1987. Angiogenic factors. Science 235 (4787), 442–447.
Gardner, L.B., Li, Q., Park, M.S., Flanagan, W.M., Semenza, G.L., Dang, C.V., 2001. Hypoxia inhibits G1/S transition through regulation of p27 expression. J. Biol. Chem. 276 (11), 7919–7926.
Hanahan, D., Weinberg, R.A., 2000. The hallmarks of cancer. Cell 100 (1), 57–70.
Hanahan, D., Weinberg, R.A., 2011. Hallmarks of cancer: the next generation. Cell 144 (5), 646–674.
Hansen, R.K., Bissell, M.J., 2000. Tissue architecture and breast cancer: the role of extracellular matrix and steroid hormones. Endocr. Relat. Canc. 7 (2), 95–113.
Hoehme, S., Drasdo, D., 2010. Biomechanical and nutrient controls in the growth of mammalian Cell populations. Math. Popul. Stud. 17 (3), 166–187.
Jiang, Y., Pjesivac-Grbovic, J., Cantrell, C., Freyer, J.P., 2005. A multiscale model for avascular tumor growth. Biophys. J. 89 (6), 3884–3894.
Li, F., Tan, H., Singh, J., Yang, J., Xia, X., Bao, J., et al., 2013. A 3D multiscale model of cancer stem cell in tumor development. BMC Syst. Biol. 7 (S2), S12.
Macklin, P., Edgerton, M.E., Thompson, A.M., Cristini, V., 2012. Patient-calibrated agent-based modelling of ductal carcinoma in situ (DCIS): from microscopic measurements to macroscopic predictions of clinical progression. J. Theor. Biol. 301, 122–140.
Macklin, P., McDougall, S., Anderson, A.R., Chaplain, M.A., Cristini, V., Lowengrub, J., 2009. Multiscale modelling and nonlinear simulation of vascular tumour growth. J. Math. Biol. 58 (4–5), 765–798.
Muthukkaruppan, V.R., Kubai, L., Auerbach, R., 1982. Tumor-induced neovascularization in the mouse eye. Journal of the National Cancer Institute 69 (3), 699–708.
Orford, K.W., Scadden, D.T., 2008. Deconstructing stem cell self-renewal: genetic insights into cell-cycle regulation. Nat. Rev. Genet. 9 (2), 115.
Panorchan, P., Thompson, M.S., Davis, K.J., Tseng, Y., Konstantopoulos, K., Wirtz, D., 2006. Single-molecule analysis of cadherin-mediated cell-cell adhesion. J. Cell Sci. 119 (1), 66–74.
Peng, L., Trucu, D., Lin, P., Thompson, A., Chaplain, M.A., 2017. A multiscale mathematical model of tumour invasive growth. Bull. Math. Biol. 79 (3), 389–429.
Perfahl, H., Byrne, H.M., Chen, T., Estrella, V., Alarcón, T., Lapin, A., Reuss, M., 2011. Multiscale modelling of vascular tumour growth in 3D: the roles of domain size and boundary conditions. PloS One 6 (4), e14790.
Ribba, B., Saut, O., Colin, T., Bresch, D., Grenier, E., Boissel, J.P., 2006. A multiscale mathematical model of avascular tumor growth to investigate the therapeutic benefit of anti-invasive agents. J. Theor. Biol. 243 (4), 532–541.
Rocha, H.L., Almeida, R.C., Lima, E.A.B.F., Resende, A.C.M., Oden, J.T., Yankeelov, T.E., 2018. A hybrid three-scale model of tumor growth. Math. Model Methods Appl. Sci. 28 (1), 61–93.
Royds, J.A., Dower, S.K., Qwarnstrom, E.E., Lewis, C.E., 1998. Response of tumour cells to hypoxia: role of p53 and NFkB. Mol. Pathol. 51 (2), 55.
Slodkowska, E.A., Cribier, B., Peltre, B., Jones, D.M., Carlson, J.A., 2010. Calcifications associated with basal cell carcinoma: prevalence, characteristics, and correlations. Am. J. Dermatopathol. 32 (6), 557–564.
Sutherland, R.M., 1988. Cell and environment interactions in tumour microregions: the multicell spheroid model. Science 240 (4849), 177–184.
Sutherland, R.M., McCredie, J.A., Inch, W.R., 1971. Growth of multicell spheroids in tissue culture as a model of nodular carcinomas. Journal of the National Cancer Institute 46 (1), 113–120.
Tyson, J.J., Novak, B., 2001. Regulation of the eukaryotic cell cycle: molecular antagonism, hysteresis, and irreversible transitions. J. Theor. Biol. 210 (2), 249–263.
Wise, S.M., Lowengrub, J.S., Frieboes, H.B., Cristini, V., 2008. Three-dimensional multispecies nonlinear tumor growth—I: model and numerical method. J. Theor. Biol. 253 (3), 524–543.
Zhang, L., Athale, C.A., Deisboeck, T.S., 2007. Development of a three-dimensional multiscale agent-based tumor model: simulating gene-protein interaction profiles, cell phenotypes and multicellular patterns in brain cancer. J. Theor. Biol. 244 (1), 96–107.